THE UNIVERSITY OF CHICAGO

MODELING OF NEMATIC LIQUID CRYSTALS UNDER THE EFFECT OF CHIRALITY, EXTERNAL FIELDS AND SURFACE CONDITIONS

A DISSERTATION SUBMITTED TO
THE FACULTY OF THE DIVISION OF THE PHYSICAL SCIENCES
IN CANDIDACY FOR THE DEGREE OF
DOCTOR OF PHILOSOPHY

DEPARTMENT OF CHEMISTRY

BY

YE ZHOU

CHICAGO, ILLINOIS

DECEMBER 2018

For my husband, Yutian Nie

TABLE OF CONTENTS

LIST OF FIGURES

ACKNOWLEDGMENTS

Time flies and it seems that all of a sudden it is time for me to say goodbye to this beautiful campus and thanks to all the people I owe my gratitude.

In the first place, I would like to thank my advisor, Prof. Juan J. de Pablo. Thanks for giving me the opportunity to join our computational chemistry research group from a background of organic chemistry in 2013. It was a very generous offer and this research group has been a warm family for me in the past five years. I am grateful to your guidance and support all along the way.

Second, I would like to give my special thank to my colleagues: Dr. Tyler Roberts, who taught me the numerical methods and basic theory of Liquid crystal; Dr. Mohammad Rahimi, who helped me with the code optimization; Dr. Jose A Martinez-Gonzalez and Dr. Rui Zhang for the valuable discussions. I am lucky to have all of you in the years of my graduate research and wish you all the best in your career.

I also owe my thanks to many other researchers who I collaborated with (in alphabetic order): Ashley Guo, Dr. Bohdan Senyuk, Dr. Emre Bukusoglu, Dr. Kunyun He, Dr. Monirosadat Sadati, Dr. Piotr Sleczkowski, Dr. Xiaoguang Wang, and Dr. Xiao Li; together with their supervisors: Prof. Emmanuelle Lacaze, Prof. Ivan Smalyukh, Prof. Paul Nealey, Prof. Nicholas L. Abbott, and Prof. Teresa Lopez Leon. I have learned a lot from all of you.

Last but not least, I have many thanks to my family and friends, especially Yutian Nie, Chun Zhou and Weiwei Chu, who have always been by my side through the good and bad.

ABSTRACT

Nematic liquid crystals (LCs) have been an area of intense investigation. In this thesis, we employ the numerical calculations based on the Landau–de Gennes theory to model nematic LC systems under the effect of chirality, external fields, and anchoring conditions.

In chapters two and three, we investigate the rich morphological behaviors in confined cholesteric liquid crystals (ChLCs), arising from the balance between elasticity, chirality, and surface energy. More specifically, a systematic study of micrometer-sized ChLC droplets and shells is presented. In ChLC droplets, with increasing chirality, a continuous transition is observed from a twisted bipolar structure to a radial spherical structure all within a narrow range of chirality. During such a transition, a bent structure is predicted by simulations and confirmed by experimental observations. The influence of chirality and surface interactions are discussed in the context of the potential use of ChLC droplets as stimuli-responsive materials for reporting molecular adsorbates. To broaden the spectrum of defect textures, the third chapter examines more complex geometries of boundaries, shells. We propose a dimensionless parameter to represent the chirality in shell geometry and characterize phase boundaries in the chirality-thickness phase diagram. Importantly, we observe that, in uniform shells, the structural transition, in response to both chirality and shell geometry, is accompanied by an abrupt change of defect positions. Its response to chirality is more sensitive compared to that of ChLC droplet with same size, implying an enhanced performance of the potential use as sensors. Moreover, we demonstrate that non-chiral and chiral nematic shells exhibit distinct equilibrium positions of inner drop in shells, which are governed by shell chirality.

In the fourth chapter, we study the effect of strong uniform magnetic field on the reorientations of the director fields and defects on tetravalent namatic liquid crystal shells. Two different cases, in terms of thickness gradient, are studied: i) homogeneous shells with four s=$+\frac{1}{2}$ defects in tetrahedral arrangement, and ii) inhomogeneous shells with four $+\frac{1}{2}$ defects localized in the thinner part of the shells. Even though the defects finally move to the poles

determined by the magnetic field in all cases, the dynamics of defect motions we observe are extremely rich and compelling. We investigated the underlying mechanism and demonstrate that the disclination walls, which depend on the direction of magnetic fields with respect to the defect orientations, are essential in determining the defect motions. Moreover, we report a hybrid-splay-bend disclination wall for the first time, to our knowledge. Our corresponding experimental observations show a good agreement with simulation results, hence validate the detailed structures of disclination walls and their evolution mechanisms.

The last chapter examines the evolution of defect configurations, including recently reported elastic hexadecapoles and other multipoles, by tuning the preferred tilt angle of degenerate conic anchoring. In order to gain a systematic understanding of hexadecapoles and other related structures, a new continuum model for anchoring is introduced here at the level of a Landau-de Gennes free energy functional. New types of angular and radial dependencies for colloidal interactions are predicted and confirmed experimentally as a function of preferred tilt angle. In particular, the new model predicts a new type of elastic dipole whose stability decreases as preferred tilt angle increases, as well as the dipole-hexadecapole transformation, which is confirmed by our experimental observations. Taken together, the results of simulations and experiments presented here suggest that new and previously unanticipated avenues may exist for design of self-assembled crystal lattice structures via control of tilt angle.

CHAPTER 1

INTRODUCTION

1.1 Nematic ordering

Liquid crystals (LCs) are states with material properties between the isotropic liquid and the fully ordered crystals. There are many different types of liquid crystal phases. Depending on how the transition between liquid crystal phases occurs, they are categorized as *thermotropic LCs* (driven by pure thermal processes) and *lyotropic LCs* (driven by the influence of solvents). In this work, we focus on the thermotropic LCs, which are mostly composed of rod-shaped anisotropic molecules. Distinct from isotropic molecules, they have alignment preference along one spatial direction with their long axes roughly parallel. Thus, when a liquid crystal phase has high degree of long-range orientational order, but no positional order, it is called the *nematic* phase (Fig 1.1b) and the direction of average molecular ordering is named as the *director* (**n**) [49].

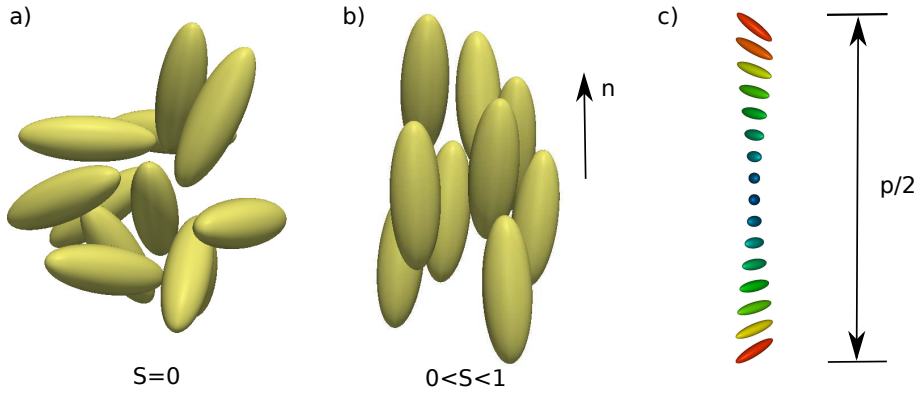

Figure 1.1: a) Isotropic phase ($S = 0$), b) nematic phase($0 < S < 1$), c) twisting helix of cholesteric LCs.

1.1.1 Scalar order parameter

To describe the orientational orders in nematic LC phases, the most common formulation uses the average of the second Legendre polynomial [49],

$$S = \langle P_2(\cos\theta)\rangle = \frac{1}{2}\left\langle 3\cos^2\theta - 1\right\rangle = \int f(\theta)\frac{1}{2}\left(3\cos^2\theta - 1\right)d\Omega, \tag{1.1}$$

where θ is the angle between the long axis of a selected molecule and the director $\mathbf{n}$; the bracket denotes the time average of the angles θ over the ensemble of molecules; $f(\theta)$ is the orientational distribution function of θ; and $d\Omega$ is the differential of the solid angle.

The value of *scalar order parameter* S varies from $-\frac{1}{2}$ to 1. It is obvious that $S = 1$ in a fully ordered state, where the molecules are perfectly aligned along $\mathbf{n}$ ($\theta = 0$ holds true for all molecules). Whereas, in a disordered isotropic phase (Fig 1.1), where the molecules are randomly oriented, $f(\theta)$ is constant and the order parameter $S = 0$ as shown in Equation 1.2.

$$S = \int f(\theta)\frac{1}{2}\left(3\cos^2\theta - 1\right)d\Omega = \frac{\int_0^\pi \frac{1}{2}\left(3\cos^2\theta - 1\right)\sin\theta d\theta \int_0^{2\pi} d\phi}{\int_0^\pi \sin\theta d\theta \int_0^{2\pi} d\phi} = 0. \tag{1.2}$$

The negative value of $S = -\frac{1}{2}$ corresponds to a state where all the molecules are aligned perpendicularly to the director, which exists only in special cases.

1.1.2 Biaxility

It is common for the nematic orientational order to exhibit biaxiality when the external fields break the rotational symmetry of the molecular orientational fluctuations around the director. From a crystallographic point of view, the symmetry of uniaxial LCs is $D_{\infty h}$, while that of biaxial LCs is D_{2h}.

The *biaxiality* is usually denoted as P. It varies between $\frac{3}{2}$ and $-\frac{3}{2}$, where $P = 0$ characterizes uniaxial ordering and $|P| = \frac{3}{2}$ corresponds to the perfect biaxial ordering along the second director $\mathbf{e}^{(1)}$, which is perpendicular to $\mathbf{n}$. Whereas the known nematic phases

are uniaxial in bulk, local biaxiality can develop in confined nematics and especially in the cores of topological defects [49]. In this thesis, we always assume a uniaxial nematic ($P = 0$), unless otherwise stated.

1.1.3 Chirality

Cholesteric liquid crystals (ChLCs), or chiral nematic liquid crystals, are LCs that favor a twisted or helical structure in the bulk (also called a cholesteric phase with a single uniform helical axis) [49, 20], as shown in Fig 1.1c. The *pitch* (p) of the helix is defined as the distance along the helical axis over which the director rotates through 2π radians. Such twisted structures can have a single uniform helical axis and reflect light selectively, thereby making cholesteric liquid crystals prospective candidates for optical devices including displays, lasers, waveguides, and resonators [40, 18].

1.1.4 Tensor representation

The tensor representation is defined as [49]

$$Q_{ij} = S(n_i n_j - \frac{1}{3}\delta_{ij}) + \frac{P}{3}(e_i^{(1)} e_j^{(1)} - e_i^{(2)} e_j^{(2)}) \tag{1.3}$$

where $i = x, y, z$ are the Cartesian components, $\mathbf{e}^{(1)}$ is the secondary director corresponding to biaxial ordering, and $\mathbf{e}^{(2)} = \mathbf{n} \times \mathbf{e}^{(1)}$.

It captures five degrees of freedom: two for director $\mathbf{n}$, one for possible biaxial axis $\mathbf{e}^{(1)}$, one for scalar order parameter S, and one for biaxility P.

The $\mathbf{Q}$ tensor has several interesting properties:

1. It is symmetric, which is obvious by its definition ($Q_{ij} = Q_{ji}$).

2. It is traceless. Since $\mathbf{n}$, $\mathbf{e}^{(1)}$, $\mathbf{e}^{(2)}$ are unit vectors, $n_i n_i = 1$, $e_i^{(1)} e_i^{(1)} = 1$, $e_i^{(2)} e_i^{(2)} = 1$,

therefore,

$$Q_{ii} = S(n_i n_i - \frac{1}{3}\delta_{ii}) + \frac{P}{3}(e_i^{(1)} e_i^{(1)} - e_i^{(2)} e_i^{(2)}) = S(1-1) + \frac{P}{3}(1-1) = 0 \qquad (1.4)$$

With properties 1 and 2, **Q** tensor has only five independent components.

3. The eigenvectors of the tensor are $\mathbf{n}$, $\mathbf{e}^{(1)}$, $\mathbf{e}^{(2)}$, with $\frac{2}{3}S$, $-\frac{S-P}{3}$, $-\frac{S+P}{3}$ as the corresponding eigenvalues.

   Knowing that $\mathbf{n}$, $\mathbf{e}^{(1)}$, $\mathbf{e}^{(2)}$ are mutually perpendicular, we have $n_i e_i^{(1)} = 0$, $n_i e_i^{(2)} = 0$, and $e_i^{(1)} e_i^{(2)} = 0$, therefore,

$$Q_{ij} n_i = \left(S(n_i n_j - \frac{1}{3}\delta_{ij}) + \frac{P}{3}(e_i^{(1)} e_j^{(1)} - e_i^{(2)} e_j^{(2)}) \right) n_i = S(n_j - \frac{1}{3} n_j) = \frac{2}{3} S n_i \quad (1.5)$$

$$Q_{ij} e_i^{(1)} = \left(S(n_i n_j - \frac{1}{3}\delta_{ij}) + \frac{P}{3}(e_i^{(1)} e_j^{(1)} - e_i^{(2)} e_j^{(2)}) \right) e_i^{(1)} = -\frac{S-P}{3} e_i^{(1)} \qquad (1.6)$$

$$Q_{ij} e_i^{(2)} = \left(S(n_i n_j - \frac{1}{3}\delta_{ij}) + \frac{P}{3}(e_i^{(1)} e_j^{(1)} - e_i^{(2)} e_j^{(2)}) \right) e_i^{(2)} = -\frac{S+P}{3} e_i^{(2)} \qquad (1.7)$$

In the case of uniaxial tensor ($P = 0$), it is easy to derive the director and order parameter from eigen-decomposition of **Q**-tensor, where S is $\frac{3}{2}$ of its largest eigenvalue and $\mathbf{n}$ is its corresponding eigenvector. The derived director is 'headless', meaning that $\mathbf{n}$ and $-\mathbf{n}$ are both eigenvectors and are the same.

1.1.5 Topological Defects

Generally speaking, defects are any discontinuity in orientations, i.e. any discontinuity in the director field $\mathbf{n}(\mathbf{r})$. It could be located on a point or on a line, in which case the defect is usually referred to as a point defect (hedgehog) or disclination line, respectively. In the nematic phase, the defect core is like a 'melt'region with low scalar order parameter. Under crossed polarizers, black brushes are observed near defects. They are regions where

the director is either parallel or perpendicular to the polarizer or analyzer. Therefore, the rate of the director rotation surrounding defect is proportional to number of black brushes, which is characterized by the strength of defect, topological charge, or winding number. Considering 2D point defect, if we keep track of the director orientations along a circular path around this defect in a clockwise mannar, the winding number is defined as the total angle of director rotation divided by 2π. A point defect with four black brushes corresponds to a winding number of 1 [49, 5] .

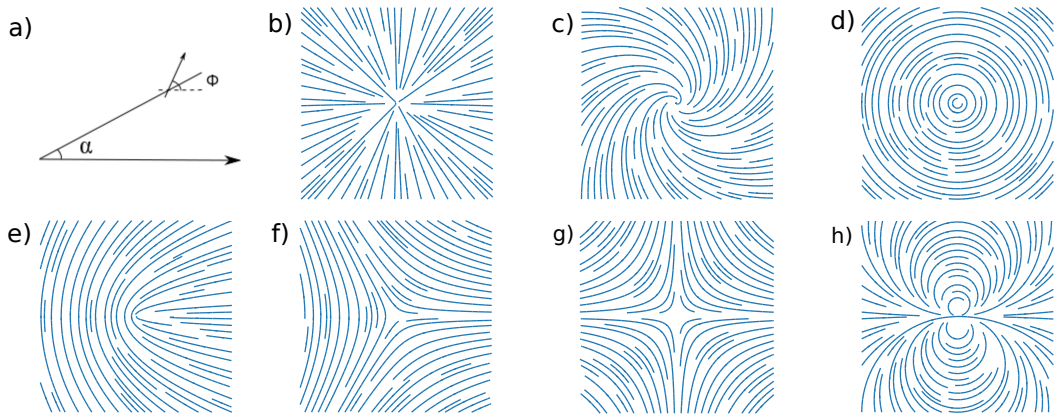

Figure 1.2: a) Director orientation (ϕ) indicated by arrow along a polar line at α. Molecular orientation near a point defect with (b) $s = 1$, $c = 0$, (c) $s = 1$, $c = \frac{\pi}{4}$, (d) $s = 1$, $c = \frac{\pi}{2}$, (e) $s = \frac{1}{2}$, $c = 0$, (f) $s = -\frac{1}{2}$, $c = 0$, (g) $s = 2$, $c = 0$ and (h) $s = 2$, $c = 0$.

It is also possible to generalize the director orientations around a 2D defect by

$$\phi = s\alpha + c \tag{1.8}$$

where $\alpha = \tan^{-1}(y/x)$ (Fig 1.2a), c is a constant, and s is the strength of defect [5].

Fig 1.2 displays some examples of molecular orientations near 2D defect with different topological charges. For $s \neq 1$, a change of c leads to a simple rotation, while for $s = 1$, the pattern itself is changed.

The energy of a 2D disclination in a circular layer of radius R and of unit thickness is

$$f_{\text{defect}} = f_c + \pi K s^2 \ln(R/r_c) \tag{1.9}$$

where f_c is the energy of the central region with radius r_c, which is unknown; K is the elastic constant (be discussed later) [5].

The expression 1.9 shows that the energy of a single defect is proportional to s^2, thus a 2D point defect with large absolute value of topological charge is unstable.

The interaction between disclinations may be calculated by superposing the solutions of the form (1.8) and is given by (assuming $r_c \ll r_{12} \ll R$),

$$f_{\text{interaction}} = \pi k(s_1 + s_2)^2 \ln(R/r_c) - 2\pi k s_1 s_2 \ln(r_{12}/2r_c) \tag{1.10}$$

where r_{12} is the separation of the defect pair.

In the case where $\sum s_i = 0$, the interaction becomes independent of R. Accordingly, driven by the second term in 1.10, the defects of like signs repel and those of opposite signs attract with each other. The force between two singularities is $2\pi k s_1 s_2 / r_{12}$, inversely proportional to the separation.

1.2 The Landau–de Gennes Theory

The Landau–de Gennes theory is a phenomenological model, where the free energy is constructed by the tensor order parameter ($\mathbf{Q}$). In general, it is composed of two contributions: the short range phase free energy and the long-range elastic free energy. Other effects, such as surface anchoring, chirality, and external fields, can be easily included by adding more free energy terms.

1.2.1 Phase energy

The nematic-isotropic transition of thermotropic LCs is first-order, where the order parameter changes discontinuously at the phase transition. To model such a transition, the phase energy is constructed by the nematic order parameter tensor.

$$f_{\text{phase}} = \frac{A}{2}\left(1 - \frac{U}{3}\right) Q_{ij}Q_{ji} - \frac{AU}{3} Q_{ij}Q_{jk}Q_{ki} + \frac{AU}{4}\left(Q_{ij}Q_{ji}\right)^2 \tag{1.11}$$

where A has the unit of energy density and is typically around 10^5 J/m^3; U is a dimensionless parameter which governs the equilibrium order parameter and the phase transition.

Assuming a uniaxial ordering, $Q_{ij} = S(n_i n_j - \frac{1}{3}\delta_{ij})$, we have $Q_{ij}Q_{ji} = \frac{2}{3}S^2$ and $Q_{ij}Q_{jk}Q_{kl} = \frac{2}{9}S^3$. The phase energy can be simplified to be a function of S,

$$f_{\text{phase}} = \frac{A}{3}\left(1 - \frac{U}{3}\right) S^2 - \frac{2AU}{27} S^3 + \frac{AU}{9} S^4 \tag{1.12}$$

The cubic term is essential here for two reasons. First, it breaks the symmetry, since S and $-S$ correspond to two distinct states. Second, without the cubic term, the phase transition becomes continuous.

The equilibrium value of the nematic order parameter could be derived by the minimization of phase energy. It should satisfy

1. $\frac{d}{dS} f_{\text{phase}} = 0$
2. $\frac{d^2}{dS^2} f_{\text{phase}} > 0$

Solving the first condition yields three possible candidates for equilibrium S, which are

$$\begin{cases} S_1 = \frac{1}{4}(1 + 3\sqrt{1 - \frac{8}{3U}}), \\ S_2 = \frac{1}{4}(1 - 3\sqrt{1 - \frac{8}{3U}}), \\ S_3 = 0. \end{cases}$$

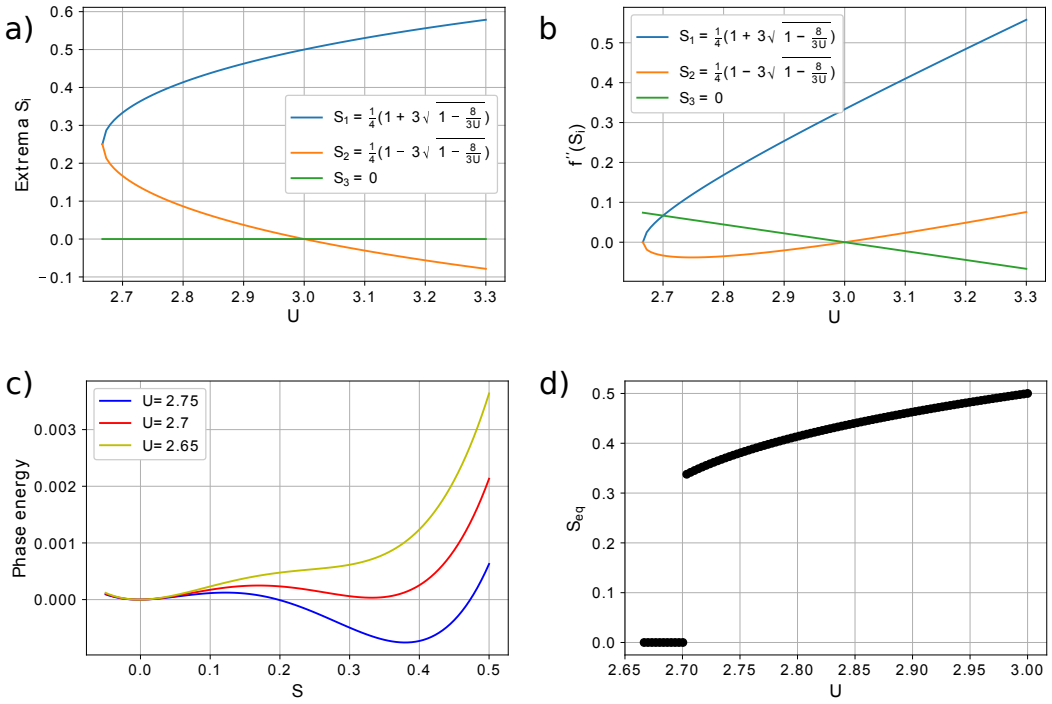

Figure 1.3: a) Values of three extrema S_i as a function of U. b) The second derivative of free energy on S at extrema S_i as a function of U. c) Phase energy as a function of order below ($U = 2.75$, blue), at ($U = 2.7$, red), above ($U = 2.65$, yellow) nematic-isotropic phase transition temperature. d) The equilibrium order parameter as a function of U. The change of S is discontinuous at phase transition ($U = 2.7$).

By examining the values of extrema S_i and the second derivative of phase energy at S_i (Fig 1.3 a and b), we have

$$S_{\text{eq}} = \begin{cases} \frac{1}{4}(1 + 3\sqrt{1 - \frac{8}{3U}}) & U > 2.7, \\ 0 & U \leq 2.7, \end{cases}$$

As discussed above, $S = 0$ corresponds to an isotropic phase. Therefore, the nematic-isotropic transition occurs at $U = 2.7$ (corresponding to the nematic-isotropic transition temperature T_{NI}). According to Fig 1.3d, this phase transition is discontinuous on S. Another interesting fact is that between $U = 2.7$ and $U = 3$, the isotropic phase ($S = 0$) and nematic phase ($S > 0$) coexist (there are two minima of phase energy). Above $U = 3$ the isotropic phase vanishes, thus $U = 3$ corresponds to the super-cooling temperature (T^*). Similarly the value of $U = \frac{8}{3}$, below which S_1 is no longer a minimum of phase energy,

relates to the super-heating temperature (T^{**}).

1.2.2 Elastic energy

The Elastic energy governs the long-range director distortions and penalizes elastic deformations [60]. It can be constructed by the spatial derivatives of either the director **n** or **Q** tensor.

Frank–Oseen director representation

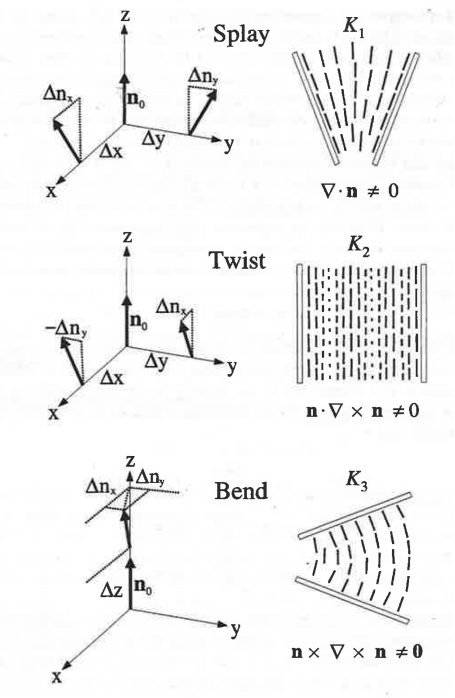

Figure 1.4: The depictions of the six basic curvature strains in Equation 1.14 (left column) and the graphic visualizations (right) of the three basic elastic deformations: splay, twist, and bend, from top to bottom rows [73].

The Frank–Oseen (FO) director representation [9] of the elastic free energy density reads,

$$\begin{aligned} f_{\mathrm{el}}^{\mathrm{FO}} =& \frac{K_1}{2}(\nabla \cdot \mathbf{n})^2 + \frac{K_2}{2}(\mathbf{n} \cdot \nabla \times \mathbf{n})^2 + \frac{K_3}{2}(\mathbf{n} \times \nabla \times \mathbf{n})^2 \\ &+ \frac{K_2 + K_4}{2}\nabla \cdot [(\mathbf{n} \cdot \nabla)\mathbf{n} - (\nabla \cdot \mathbf{n})\mathbf{n}] \end{aligned} \tag{1.13}$$

where the Frank elastic constants K_1, K_2, and K_3 represent three basic deformation modes: splay, twist, bend, respectively; the combination of $(K_2 + K_4)$ is called the saddle-splay constant, which is usually omitted when considering strong anchoring, since it can be transformed to a surface term via the divergence theorem.

These three basic deformation modes can be expressed using $\mathbf{n}_0 = (0, 0, 1)$ parallel to z at the origin in a local right-handed system of Cartesian coordinate. Here we notify $\frac{\partial n_i}{\partial j}$ by $n_{i,j}$. Since $\mathbf{n} \cdot \mathbf{n} = 1$, it follows that $\mathbf{0} = \nabla(\mathbf{n} \cdot \mathbf{n}) = 2\mathbf{e}_j n_i n_{i,j}$. Thus, $n_i n_{i,j} = 0$, and for $\mathbf{n}_0 = (0, 0, 1)$, $n_{z,j} = 0$.

As shown in Fig 1.4, the three elastic components are:

$$\text{Splay}: n_{x,x},\, n_{y,y}; \quad \text{Twist}: n_{x,y},\, -n_{y,x}; \quad \text{Bend}: n_{x,z},\, n_{y,z}. \tag{1.14}$$

It relates to the terms in equation 1.13 by,

$$\nabla \cdot \mathbf{n} = n_{x,x} + n_{y,y}, \tag{1.15}$$

$$\mathbf{n} \cdot \nabla \times \mathbf{n} = n_{y,x} - n_{x,y}, \tag{1.16}$$

$$(\mathbf{n} \times \nabla \times \mathbf{n})^2 = n_{y,z}^2 + n_{x,z}^2 \tag{1.17}$$

One weakness of the FO expression is that it diverges near defect regions, and this is where the tensor representation outperforms the director representation.

Tensor representation

The tensor representation for elastic free energy is

$$f_{\text{el}} = \frac{L}{2} \frac{\partial Q_{ij}}{\partial x_k} \frac{\partial Q_{ij}}{\partial x_k} \tag{1.18}$$

where parameter L represents the elastic constant.

In a uniaxial system with spatially invariant scalar order ($\nabla S = 0$), the free energy can

be rewritten in terms of $\mathbf{n}$:

$$\begin{aligned} f_{\text{el}} &= LS^2(\nabla \mathbf{n})^2 \\ &= LS^2[(\nabla \cdot \mathbf{n})^2 + (\mathbf{n} \cdot \nabla \times \mathbf{n})^2 + (\mathbf{n} \times \nabla \times \mathbf{n})^2 + \nabla \cdot [(\mathbf{n} \cdot \nabla)\mathbf{n} - (\nabla \cdot \mathbf{n})\mathbf{n}]] \end{aligned} \tag{1.19}$$

The expression 1.19 is the same as the Frank–Oseen director representation (1.13) under the one-constant assumption, $K_1 = K_2 = K_3 = K_2 + K_4 = K = 2LS^2$. For 5CB nematic, the elastic constants are on the order of pN and they differ from the average by about 40%. In our simulation, the one-constant assumption is commonly used to simply the calculations.

In general, more terms could be included, in order to incorporate all three modes.

$$f_{\text{el}} = \frac{L_1}{2}\frac{\partial Q_{ij}}{\partial x_k}\frac{\partial Q_{ij}}{\partial x_k} + \frac{L_2}{2}\frac{\partial Q_{ij}}{\partial x_j}\frac{\partial Q_{ik}}{\partial x_k} + \frac{L_3}{2}Q_{ij}\frac{\partial Q_{kl}}{\partial x_i}\frac{\partial Q_{kl}}{\partial x_j} \tag{1.20}$$

where the mappings between L_i and K_i (assuming $K_4 = 0$) are:

$$\begin{aligned} L_1 &= \frac{1}{6S^2}(K_3 - K_1 + 3K_2) \\ L_2 &= \frac{1}{S^2}(K_1 - K_2) \\ L_3 &= \frac{1}{2S^3}(K_3 - K_1) \end{aligned} \tag{1.21}$$

Splay-bend order parameter

The splay-bend parameter, $S_{\text{SB}} = \frac{\partial^2 Q_{ij}}{\partial x_i \partial x_j}$, is used to capture splay and bend deformations of the director field [6]. Assuming that there is no spatial variance in scalar order ($\nabla S = 0$), S_{SB} in the director field representation is

$$S_{\text{SB}} = \frac{3S}{2}\nabla(\mathbf{n}(\nabla \cdot \mathbf{n}) - \mathbf{n} \times \nabla \times \mathbf{n}) \tag{1.22}$$

The two terms in Equation (1.22) are related to the splay and bend deformations in the FO expression. Large positive values of S_{SB} implies strong splay deformation, likewise for large

negative values and bend deformation.

Chirality

The elastic free energy for cholesteric liquid crystals is

$$f_{\text{el,chol}}^{\text{FO}} = \frac{K_1}{2}(\nabla \cdot \mathbf{n})^2 + \frac{K_2}{2}(\mathbf{n} \cdot \nabla \times \mathbf{n} + q_0)^2 + \frac{K_3}{2}(\mathbf{n} \times \nabla \times \mathbf{n})^2 \tag{1.23}$$

where $q_0 = \frac{2\pi}{p}$ is denoted as the wave vector, which quantifies the system's chirality (for a non-chiral system $q_0 = 0$). Driven by the second term (twist deformation), the liquid crystal favor a twisted or helical structure in the bulk with period $p = \frac{2\pi}{q_0}$ [49].

The tensor representation under one-constant assumption reads,

$$f_{\text{el,chol}} = \frac{L}{2}\frac{\partial Q_{ij}}{\partial x_k}\frac{\partial Q_{ij}}{\partial x_k} + 2q_0 L \epsilon_{ikl} Q_{ij}\frac{\partial Q_{lj}}{\partial x_k} \tag{1.24}$$

where ϵ_{ikl} is the Levi-Civita tensor.

1.2.3 Surface energy

Interfaces influence the orientations and orderings in different way and this effect is called anchoring. There are mainly two type of anchorings: planar degenerate anchoring, where the surface molecules favor a tangential alignment with no in-plane preference, and homeotropic anchoring, where the surface molecules favor a perpendicular ordering with respect to surface (Fig 1.5a).

In the literature, the uniform surface anchoring is usually modeled by Rapini-Papoular-like surface free energy [45].

$$f_{\text{surf}}^{h} = \int_{\text{surf}} \frac{W_h}{2}\left(Q_{ij} - Q_{ij}^0\right)^2 d\Sigma. \tag{1.25}$$

where W_h is the anchoring strength, which generally range from 10^{-7} to 10^{-3} J/m^2. The

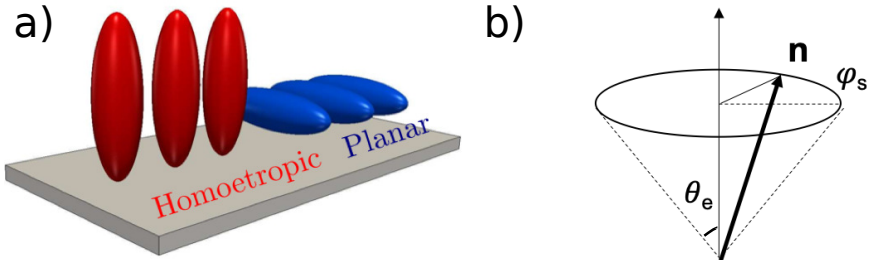

Figure 1.5: Schematic representation of a) homeotropic (red), planar anchoring (blue) and b) degenerate conic anchoring.

preferred order parameter tensor at the surface, corresponding to a surface director aligned with the easy axis, is denoted by Q^0_{ij} [45]. Such a model is capable of describing the monostable anchoring with arbitrary easy axes $\mathbf{n}_e$ by penalizing quadratically any deviations of the director $\mathbf{n}$ from $\mathbf{n}_e$. When the easy axis is along the surface normal, Equation 1.25 yields a homeotropic anchoring condition. When n_e is parallel to the interface, it is usually referred to as non-degenerate planar anchoring. It differs from degenerate planar anchoring in a way that molecules prefer to align along an in-plane direction at the interface.

The free energy functional for planar degenerate anchoring was introduced by Fournier and Galatola [12]:

$$f^p_{\text{surf}} = \int_{\text{surf}} W_p \left(\tilde{Q}_{ij} - \tilde{Q}^{\perp}_{ij}\right)^2 d\Sigma. \tag{1.26}$$

The surface free energy for degenerate planar anchoring is constructed with the aid of a projection operator $P_{ij} = \delta_{ij} - \nu_i\nu_j$, defined with a surface normal ν_i. The term $\tilde{Q}^{\perp}_{ij} = P_{ik}\tilde{Q}_{kl}P_{lj}$ is the projection of $\tilde{Q}_{ij} = Q_{ij} + \frac{1}{3}S_{\text{eq}}\delta_{ij}$ onto the surface [12].

To better understand the surface energy in tensor representation, we perform a transformation assuming an uniaxial order and $n_i\nu_i = \cos\theta_s$, where θ_s is the angle between surface director and surface normal.

For homeotropic anchoring, $Q^0_{ij} = S(\nu_i\nu_j - \frac{1}{3}\delta_{ij})$ and

$$\left(Q_{ij} - Q^0_{ij}\right)^2 = \left(S(n_in_j - \frac{1}{3}\delta_{ij}) - S(\nu_i\nu_j - \frac{1}{3}\delta_{ij})\right)^2 \tag{1.27}$$

$$= S^2(n_in_j - \nu_i\nu_j)^2 \tag{1.28}$$

$$= 2S^2 \sin^2\theta_s. \tag{1.29}$$

For degenerate planar anchoring,

$$\left(\tilde{Q}_{ij} - \tilde{Q}^{\perp}_{ij}\right)^2 = S^2\left(n_in_j - (\delta_{ik} - \nu_i\nu_k)n_kn_l(\delta_{lj} - \nu_l\nu_j)\right)^2 \tag{1.30}$$

$$= S^2(\nu_in_j\cos\theta_s + n_i\nu_j\cos\theta_s - \nu_i\nu_j\cos^2\theta_s)^2 \tag{1.31}$$

$$= S^2(1 - \sin^4\theta_s). \tag{1.32}$$

The transformation reveals the fact that the surface free energies f^h_{surf}, f^p_{surf} are minimized when $\theta_s = 0$ (homeotrpic anchoring) and $\pi/2$ (degenerate planar anchoring), respectively.

The strength of the uniform surface anchoring can also be interpreted by the Kleman–de Gennes extrapolation length ξ_s. It is defined as $\xi_s = K/W$, where K is the effective Frank elastic constant. It measures the relative strength of nematic elasticity with respect to surface anchoring. The extrapolation length of strong anchoring ($W \sim 10^{-3}\,\text{J/m}^2$) for a typical nematic ($K \sim 10\,\text{pN}$) is at the order of 10 nm, and that of weak anchoring ($W \sim 10^{-6}\,\text{J/m}^2$) is about 10 μm.

A special type of anchoring, called the degenerate conic anchoring (Fig 1.5b), will be discussed in Chapter 5.

1.2.4 Energy Induced by External Fields

For an anisotropic material, the electric displacement $\mathbf{D} = \epsilon_0 \epsilon \mathbf{E}$, where ϵ_0 is the *dielectric vacuum permittivity constant*, ϵ is the *dielectric tensor*. For uniaxial system, it is written as

$$\begin{bmatrix} \epsilon_\perp & 0 & 0 \\ 0 & \epsilon_\perp & 0 \\ 0 & 0 & \epsilon_\parallel \end{bmatrix} \tag{1.33}$$

where $\epsilon_\parallel$, $\epsilon_\perp$ denote the *relative dielectric permittivities*, also called *dielectric constants*, of the liquid crystal when the field and director are parallel and perpendicular, respectively. For nematic director $\mathbf{n}_0$, the electric displacement is

$$\begin{aligned} \mathbf{D} &= \epsilon_0 \epsilon \mathbf{E} \\ &= \epsilon_0 \epsilon_\parallel (\mathbf{E} \cdot \mathbf{n}_0)\mathbf{n}_0 + \epsilon_0 \epsilon_\perp [\mathbf{E} - (\mathbf{E} \cdot \mathbf{n}_0)\mathbf{n}_0] \\ &= \epsilon_0 \epsilon_\perp \mathbf{E} + \epsilon_0 \epsilon_a (\mathbf{E} \cdot \mathbf{n}_0)\mathbf{n}_0 \end{aligned} \tag{1.34}$$

where $\epsilon_a = \epsilon_\parallel - \epsilon_\perp$ is called the *dielectric ansiotropy* of the liquid crystal.

The total electric energy is [73],

$$f_{\text{elec}} = -\frac{1}{2}\mathbf{D} \cdot \mathbf{E} = -\frac{1}{2}\epsilon_0 \epsilon_\perp E^2 - \frac{1}{2}\epsilon_0 \epsilon_a (\mathbf{E} \cdot \mathbf{n})^2 \tag{1.35}$$

For nematic materials of positive ϵ_a, the f_{elec} is minimized when the $\mathbf{n}$ and $\mathbf{E}$ are parallel, and when $\epsilon_a < 0$, it is minimized when $\mathbf{n}$ is perpendicular to $\mathbf{E}$.

Within the LdG theory framework, the dielectric coupling between the non-polar nematic and an external electric field is,

$$f_{\text{elec}}^{Q} = -\frac{1}{2}\epsilon_0 \left(\bar{\epsilon} E_i^2 + \frac{\epsilon_a Q_{ij} E_i E_j}{S} \right) \tag{1.36}$$

where $\bar{\epsilon} = (2\epsilon_\perp + \epsilon_\parallel)$ is the average liquid crystal permittivity. It is the equivalent to

expression 1.35 as shown below,

$$\begin{aligned} f^{Q}_{\text{elec}} &= -\frac{1}{2}\epsilon_0 \left(\bar{\epsilon} E_i^2 + \frac{\epsilon_a Q_{ij} E_i E_j}{S} \right) \\ &= -\frac{1}{2}\epsilon_0 \left(\bar{\epsilon} E_i^2 + \epsilon_a (n_i n_j - \frac{1}{3}\delta_{ij}) E_i E_j \right) \\ &= -\frac{1}{2}\epsilon_0 \left(\bar{\epsilon} E_i^2 + \epsilon_a \left((n_i E_i)^2 - \frac{1}{3} E_i^2 \right) \right) \\ &= -\frac{1}{2}\epsilon_0 \epsilon_\perp E^2 - \frac{1}{2}\epsilon_0 \epsilon_a (\mathbf{E} \cdot \mathbf{n})^2. \end{aligned}$$

In the case where the electric field is invariant, the first term may be neglected.

The external magnectic field couples with nematic LCs in a similar way, with dielectric constant replaced by diamagnetic constant. As discussed above, when the diamagnetic anisotropy $\chi_a > 0$, the director aligns itself parallel or anti-parallel with respect to the field direction. A region of parallel alignment and anti-parallel alignment can be separated by a wall inside which the director turns through an angle π, which is named as the Helfrich walls [5]. There are three types:

- A twist wall (Fig 1.6a): the director is confined in y-z plane and twist along x-axis. The wall is parallel to the field direction.

- A bend-splay wall (Fig 1.6b): the director is confined in x-z plane. The transition from $+\mathbf{n}$ to $-\mathbf{n}$ takes place mainly through bend distortions, though some splay exist. The wall is parallel to the field direction.

- A splay-bend wall (Fig 1.6c): the director is confined in x-z plane, and the transition from $+\mathbf{n}$ to $-\mathbf{n}$ is mainly through splay distortions with some bend as well. The wall is perpendicular to the field direction.

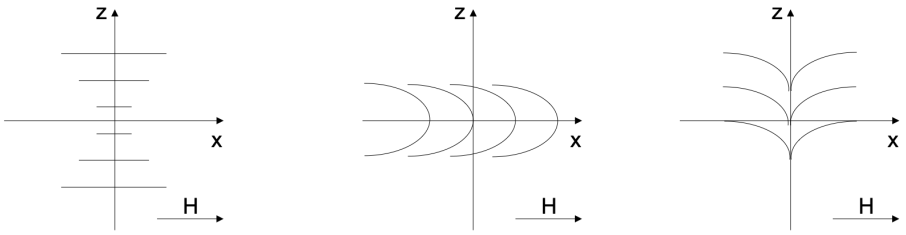

Figure 1.6: Schematic representation of Helfrich walls with field along z-axis: a) a twist wall; b) a bend-splay wall; c) a splay-bend wall

1.3 Numerical details

1.3.1 Free energy minimization

The free energy is minimized by the Euler-Lagrange equation for bulk and surface of the nematic:

$$\frac{\partial f}{\partial Q_{ij}} - \nabla \frac{\partial f}{\partial \nabla Q_{ij}} = 0 \quad \text{(bulk)}, \tag{1.37}$$

$$\frac{\partial f}{\partial \nabla Q_{ij}} \cdot \boldsymbol{\nu} = 0 \quad \text{(surface)}. \tag{1.38}$$

Applying Equations 1.37 and 1.38 to the Landau-de Gennes free energies (phase energy, elastic energy, Rapini-Papoular surface energy and Fournier-Galatola surface energy) with a symmetric-traceless operator yields:

$$\begin{aligned} h_{ij}^{\text{bulk}} = & -A\left(1-\frac{U}{3}\right)Q_{ij} + AU\left[Q_{ik}Q_{kj} - Q_{mn}Q_{nm}\left(Q_{ij}+\frac{\delta_{ij}}{3}\right)\right] \\ & + L\frac{\partial^2 Q_{ij}}{\partial x_k \partial x_k} = 0, \end{aligned} \tag{1.39}$$

$$
\begin{aligned}
h_{ij}^{\text{surf}} =& L\frac{\partial Q_{ij}}{\partial x_k}\nu_k \\
&+ W_h(Q_{ij} - Q_{ij}^0) \\
&+ 2W_p\left(\tilde{Q}_{ij} - \tilde{Q}_{ij}^{\perp} - \frac{\delta_{ij}}{3}(\nu_m\tilde{Q}_{mn}\nu_n)\right) = 0.
\end{aligned} \tag{1.40}
$$

Here the symmetric-traceless operator (Π) is defined as,

$$
\Pi(\mathbf{A}) = \frac{1}{2}(\mathbf{A} + \mathbf{A}^{\mathrm{T}}) - \frac{1}{3}\mathrm{Tr}(\mathbf{A})\boldsymbol{\delta}, \tag{1.41}
$$

where $\mathbf{A}$ is any second-order tensor and the superscript T denotes the transpose of the tensor.

1.3.2 Discretization

In most cases, it is extremely complicated to solve the above equations (1.39 and 1.40) analytically. Therefore, we turn to numerical approaches and in this work we focus on the finite difference method. The order parameter tensor is spatially discretized on a cubic mesh with uniform mesh density. The mesh resolution is determined by the nematic correlation length (ξ_N).

Taking a one dimensional function $\phi(x)$ as a simplified example, the derivatives are approximated by a second order central difference,

$$
\phi' \approx \frac{\phi(x+\Delta x) - \phi(x-\Delta x)}{2\Delta x} \tag{1.42}
$$

$$
\phi'' \approx \frac{\phi(x+\Delta x) + \phi(x-\Delta x) - \phi(x)}{\Delta x^2} \tag{1.43}
$$

For a mesh point on surface, the first derivative is estimated as

$$
\phi' \approx \frac{-\phi(x+2\Delta x) + 4\phi(x+\Delta x) - 3\phi(x)}{2\Delta x} \tag{1.44}
$$

An iterative-Ginzburg–Landau (GL) relaxation is used to iteratively solve the equations

by adding a relaxation coordinate t:

$$Q_{ij}^{t+\Delta t} = Q_{ij}^{t} + \frac{\Delta t}{\Gamma} h_{ij}. \tag{1.45}$$

where h_{ij} stands for either the bulk or surface expression (1.39 and 1.40), Δt is time step between two iterations, and Γ is a numerical relaxation constant, also known as the rotational viscosity (or diffusion) coefficient [56]. The choice of Δt should be careful. When Δt is too large, the simulation may not be able to converge, and if it is too small, the convergence will take too long.

1.3.3 Ansatz

In order to ensure the formation of specific configurations and to speed up the relaxation process, predefined initial conditions may be used in this thesis.

ChLC droplets with parallel surface anchoring

The analytical solutions of director profile for ChLC droplets with degenerate planar anchoring were discussed in 1992 [1]. In spherical coordinates, the rotation of the director along the helical axis (e_r) can be described as:

$$\mathbf{n} = \cos\Omega \mathbf{e}_\theta + \sin\Omega \mathbf{e}_\phi \tag{1.46}$$

where $\Omega = \Omega(\mathbf{r}, \theta, \phi)$. Replacing $\mathbf{n}$ in the Frank free energy (1.23) with the above ansatz (1.46) under the one-constant assumption yields,

$$f = \frac{K}{2}[(1 + \Omega_\theta^2 \sin^2\theta + \Omega_\phi^2 + 2\Omega_\phi \cos\theta)/(r\sin\theta)^2 + (\Omega_r - q)^2] \tag{1.47}$$

where subscripts r, θ, ϕ denotes corresponding derivatives. A minimization leads to a general solution:

$$\Omega = (s_0 - 1)\phi + \Omega_0 + qr \tag{1.48}$$

where s_0, Ω_0 are constants. The solutions with $s_0 = 0$ and 1 are used as the ansatz for two representative structures: diametrical spherical structure (DSS) and radial spherical structure (RSS).

Dipolar configuration

For nematic colloids with dipolar director configuration, the initial tensor profile from a multipole expansion is used:

$$\boldsymbol{n} = \boldsymbol{n}_0 + aR^2 \frac{\boldsymbol{r} - \boldsymbol{r}_{\text{col}}}{|\boldsymbol{r} - \boldsymbol{r}_{\text{col}}|^3} \tag{1.49}$$

where $\boldsymbol{n}_0$ is the unit vector for the far-field director; $a = 2.1$ is a constant, determining the initial position of the point defect; R is the colloidal radius; $\boldsymbol{r}$ is the position vector for the current position, and $\boldsymbol{r}_{\text{col}}$ is the position vector for the colloid center. The plus sign between the two terms defines the direction of the dipole. [12]

1.3.4 Reduced unit

To avoid the errors associated with working with extremely large or small numbers, all the evolution and free-energy equations are rewritten in terms of reduced units. This is done by reducing those equations by some scale natural to the problem.

Length

In our simulation, the length is scaled by a characteristic length, known as the *nematic correlation length*,

$$\xi_N \sim \sqrt{\frac{L}{A}}, \quad \hat{x} = \frac{x}{\xi_N} \tag{1.50}$$

where $\hat{x}$ is the dimensionless length.

The nematic correlation length determines the spatial scale for the variation of the nematic degree of order and estimates the size of defect. For 5CB, this length is roughly $\xi_N \sim 10$ nm. Based on the numerical parameters used in this work, $A = 1.17 \times 10^5\,\mathrm{J/m^3}$ and $L = 6 \times 10^{-12}\,\mathrm{N}$, the resulting $\xi_N = 7.15\,\mathrm{nm}$. In simulation, we choose the mesh size to be one nematic correlation length (spacing between two adjacent mesh points is $\Delta\hat{x} = 1$) to simply the calculations.

Anchoring

The dimensionless anchoring is determined by the ratio of the coherence length to the the Kleman–de Gennes extrapolation length ξ_s,

$$\hat{W} = \frac{\xi_N}{\xi_W} = \frac{W}{\sqrt{LA}}. \tag{1.51}$$

Time

The time scale is reduce by

$$t^* = \frac{\gamma \xi_N^2}{L}. \tag{1.52}$$

With the empirical viscosity γ for 5CB around $0.1\,\mathrm{J/m^3 \cdot s}$, the characteristic time $t^* \sim 1\,\mu s$.

Electric field

The electric field is scaled by

$$E^* = \sqrt{\frac{L}{\xi_N^2 \epsilon_0 \epsilon_a}}. \tag{1.53}$$

where the dielectric vacuum permittivity constant $\epsilon_0 = 8.85\,\mathrm{F/m}$; for 5CB the values for the dielectric anisotropy ϵ_a are between 8 and 11 (our calculations use the value of 10); the value of E^* we use in your calculations is around $3.64 \times 10^7\,\mathrm{V/m}$.

1.3.5 Polarized light micrographs

Polarized light micrographs were calculated using the Jones matrix formalism, in which light traverses along a chosen direction and the total phase shift is accumulated [47].

CHAPTER 2

CHOLESTERIC LIQUID CRYSTAL DROPLETS

2.1 Introduction

Cholesteric liquid crystals (ChLCs), or chiral nematic liquid crystals, are LCs that favor a twisted or helical structure in the bulk (also called a cholesteric phase with a single uniform helical axis) [20]. When confined into spherical droplets, the equilibrium configurations that ChLCs adopt can differ considerably from those in the bulk. The equilibrium free energy of such systems is governed by a subtle balance between chirality (intrinsic periodicity), bulk elasticity and surface anchoring [1]. The concentric periodicity in ChLC droplets has inspired the design of various micro-3D optical devices, including micro-resonators, micro-lasers and waveguides [18, 40]. The so-called blue phases of liquid crystals represent a distinct state that arises when the LC is highly chiral [20], and blue-phase droplets have received considerable attention in the recent literature [19, 3, 34].

Nematic liquid crystals are highly responsive to external cues applied through an interface. The sensitivity of LC droplet ordering to analytes at picogram/milliliter concentrations has provided the basis for development of sensing devices for biotoxins[25], and recent work has demonstrated ordering transitions within LC droplets triggered by the interaction with adsorbates [35]. Computational studies have also shown that surface active molecules influence the internal structure of LC droplets, giving rise to formation of intriguing self-assembled patterns [17, 36]. At longer length scales, LC droplets have also been shown to induce the interfacial self-assembly of nanoparticles, thereby providing a strategy for facile synthesis of patchy micro-particles [79, 78, 53]. Importantly, however, a majority of work to date with LC droplets has focused on nematic systems. Much less is known about the response of ChLCs to interfacial conditions, and their potential use for sensing applications has not been explored.

Experiments indicate that the radial spherical structure (RSS) (also known as the spherulitic

texture or the Frank-Pryce model) is commonly observed in ChLC droplets with planar anchoring [23, 2, 80]. For low chirality materials or small droplets, however, the twisted bipolar structure (TBS) is more energetically favorable [80]. More recently, by relying on continuum simulations of ChLC droplets and director-field ansatze [60], researchers have analyzed the structures and the corresponding free energies of six plausible structures. Their results suggest that for ChLC droplets with strong planar anchoring, TBS and RSS are the most stable structures for low and high chirality, respectively, in agreement with experimental data. Of particular interest to this work is the transition between TBS and RSS, which is of particular significance for development of adsorption-induced morphological transformations in ChLC droplets. Isolated measurements have provided a few insights into such a transition[80, 48] but, as shown in what follows, important details remain unknown.

In order to address this gap in the literature, in this chapter we present a systematic study of the effects of parallel anchoring strength and chirality on micrometer-sized ChLC droplets. To do so, we rely on a Landau–de Gennes model and a tensorial description of the local order. First, we focus on the transition process from TBS to RSS. We find a bent structure for systems with intermediate chirality, which results from the competition between elasticity and chirality. Second, we explore the impact of anchoring on the ordering of ChLC droplets. For weak anchoring, a structure similar to the bulk helical phase is found to be stable. As anchoring strength is increased, however, the quasi-helical phase gradually evolves into a planar bipolar structure (PBS), followed by a bent structure.

2.2 Model and Methods

2.2.1 Simulation details

The numerical parameters used in this chapter are $A = 1.17 \times 10^5\,\mathrm{J/m^3}$, $U = 5$, $L = 6 \times 10^{-12}\,\mathrm{N}$. The droplet radius is held constant at 715 nm. Past work on non-chiral nematic droplets suggests that LC ordering under spherical confinement is size-dependent [16]. Here,

we take into account size effects by representing the chirality in terms of the radius-to-pitch ratio ($N = 4R/p$). Here N approximates the number of π-turns of the director along the diametrical axis of the droplet.

Past numerical studies of ChLC droplets have relied on director field ansatze, which are particularly helpful for numerical simulations of high-chirality systems [60]. In this work, however, we use a random director field as an initial condition for two reasons, unless specified otherwise. First, for intermediate chirality, we cannot assume that the stable configurations will be similar to the RSS Ansatz. Thus, using the RSS Ansatze, may bias our results. Second, a pure tangential director field (with no radial component) is assumed in the RSS ansatz; this is a good approximation for ChLC droplets with strong anchoring [1], but it may not be valid for weak anchoring. In our simulations, 2 to 12 different random initial configurations are used for each set of parameters, and several metastable states are typically found for high chirality ($N > 3.5$).

For convenience, we control the location of surface defects by introducing two nanoparticles at the interface of the ChLC droplet. Previous work has demonstrated that colloidal particles have an affinity for disclination regions [50, 67, 79], where they help reduce the elastic energy. In simulations with fixed nanoparticles, defect regions tend to be captured by the nanoparticles. Therefore, by controlling their positions, one can manipulate the droplet morphology, explore the corresponding free energy landscape, and identify relevant stable and metastable states. The parameters for the nanoparticles employed here are $R_p = 71.5$ nm and no anchoring energy penalty. Due to their small size and vanishing anchoring strength, they do not influence the structure of the underlying LC, and we therefore assume that the analysis of nanoparticle-controlled droplet configurations provides a reliable means of exploring the transition mechanism that arises in pure droplets.

2.2.2 Experiment details

In our experiments, cholesteric LC systems of varying chirality were produced by addition of different concentrations of chiral dopants to nematic LC. Cholesteric LC mixtures were prepared by mixing 4-cyano-4'- pentylbiphenyl (5CB) and the chiral dopant 4-(1-methylheptyl-oxycarbonyl) phenyl-4-hexyloxybenzoate (S-811) with toluene as co-solvent. Desired amounts of S-811, 5CB and toluene were mixed using an ultrasonic cleaner. Toluene was then evaporated overnight under vacuum at 50°C. Chiral LC mixtures were kept in the isotropic phase before preparing the emulsions. To prepare emulsions, the chiral LC mixture was emulsified in Milli-Q water at ~ 50°C using a homogenizer (T25 digital ULTRA-TURRAX) equipped with a S25 N-10G dispersing element (IKA) for 30 s at 6500 rpm. Next, the emulsions were cooled down to room temperature. This method generated droplets with sizes ranging from $\sim 1\,\mu$m to $\sim 80\,\mu$m in diameter. In some experiments, colloidal particles of $1\,\mu$m-in-diameter ($8\,\mu$L from stock) were added and homogenized for an additional 20 s to facilitate adsorption of the colloids at the droplet interfaces. Micrographs of the droplets were collected using an Olympus IX71 inverted microscope (Center Valley, PA) equipped with a 100x oil-immersion objective. Bright field and polarized light images of LC-in-water emulsions were obtained with a Hamamatsu 1394 ORCA ER CCD camera (Bridgewater, NJ). Pitch sizes were determined by measuring the periodicity of the fingerprint patterns using imageJ, public domain image processing software developed by National Institutes of Health (Maryland, USA).

2.3 Results and Discussion

2.3.1 Structural Transition Induced by Increasing Chirality

As a means to establish the validity of our calculations, we begin by examining the structure of non-chiral droplets with strong anchoring ($W = 2.5 \times 10^{-3}\,\mathrm{J/m^2}$). Consistent with past literature results [60], our simulations indicate that non-chiral nematic droplets ($N = 0$)

adopt a bipolar structure (BS), with two boojums at the antipodal positions. With increasing chirality, the BS conformation evolves into a twisted bipolar structure (TBS) for low chirality ($N \leq 3.3$), with unchanged surface point defect positions. For high chirality, a radial spherical structure (RSS) with spherical symmetry becomes more energetically favorable.

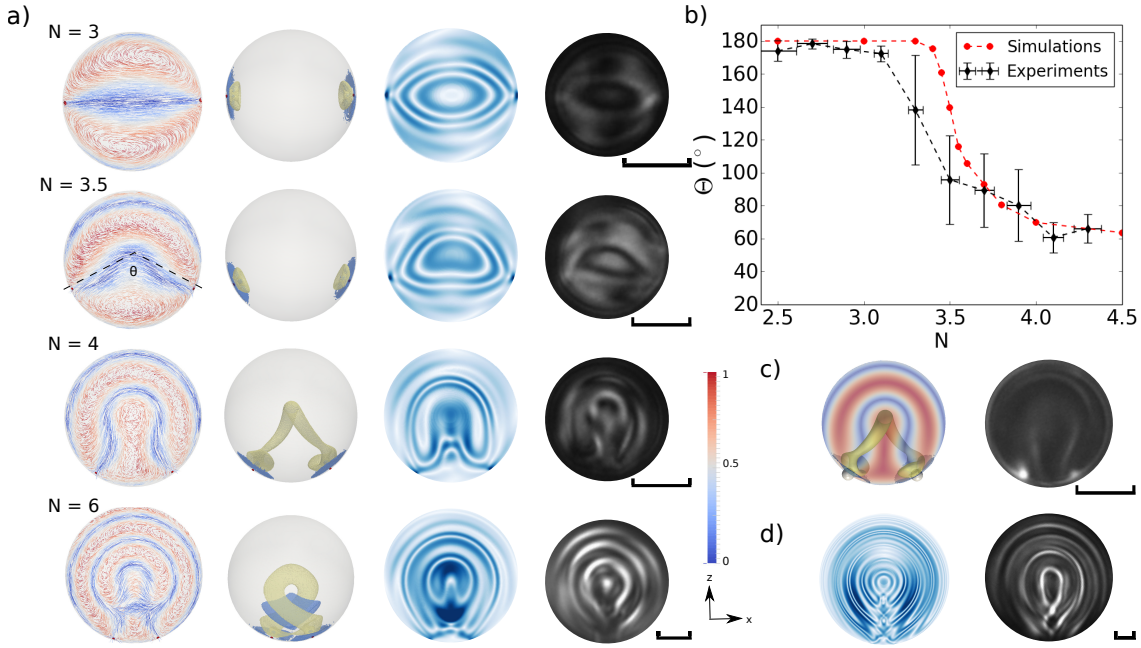

Figure 2.1: a) The four rows show results corresponding to $N = 3, 3.5, 4$ and 6, respectively. Column 1: director fields of ChLC droplets for various values of N. Point defects are shown in red (isosurface for $S = 0.5$). The director field is colored according to its projection onto the y-axis. In the image corresponding to N = 3.5, the dashed lines connect two surface point defects with the center of the droplet. The angle between these two dashed lines is defined as θ. Column 2 : splay-bend isosurfaces of ChLC droplets. The splay elastic distortion is shown in black (blue online) ($S_{\mathrm{SB}} > 0.0014$) and the bend elastic distortion is shown in grey (yellow online) ($S_{\mathrm{SB}} < -0.0014$). Column 3: polarization graphs obtained for incident light along the y-axis. Column 4: experimental images for droplets of different chirality. b) Dependence of θ on N. c) Positioning of two colloids at the surface defects of droplet with $N = 3.9$ (left: simulation, right: combined fluorescence and bright field micrographs). d) Simulated polarization graph and experimental image for RSS droplet (N = 10). (Scalar bar: $5\,\mu$m.)

To explore the transition from TBS to RSS induced by chirality, we examine the director fields of ChLC droplets for N between 3 and 6 (Fig 2.1a). As the chirality increases from $N = 3.3$, the two point defects are no longer antipodal (as in TBS), and the cylindrical

symmetry disappears. The increase of chirality leads to the formation of a bent structure. We define the angle between the two lines connecting the surface point defects to the center of the droplet as θ. For TBS, the two point surface defects are positioned diametrically ($\theta = 180°$), while for RSS, θ is below 60°. Fig 2.1b shows the variation of θ as a function of chirality (N). For $N \leq 3.3$, the TBS structure is the most stable, with $\theta = 180°$. For high chirality ($N > 4.0$), the RSS structure emerges, with $\theta \leq 90°$. In a very narrow window of chirality ($3.3 \leq N \leq 4.0$), a drastic decrease of θ is observed, providing evidence of an underlying structural transformation.

The distribution of splay and bend distortions during the transition from TBS to RSS are also shown in Fig 2.1a, using the splay-bend parameter S_{SB} (additional details are provided in the SI). For $N = 3$, both splay and bend distortions emerge near the antipodal point defects. As the chirality (N) increases, the splay and bend distortions change positions, along with the point defects. From $N = 4$, a bridge of bend distortion forms between the two point defects. As N increases, the bend disclination line fuses into a double helix.

The experimental polarized light micrographs of the droplets shown in the right column of Figure 1a are consistent with the corresponding simulated polarized light micrographs (third column in Figure 1a). Figure 1b shows the experimentally determined positions of the two surface defects on droplets of 1 wt% S-811 in 5CB dispersed in water as a function of N along with the results of our simulations. A comparison of the experiments and simulations reveals good agreement.

We emphasize here that this transition occurs within a narrow range of chirality; the sharpness of the transition could be used as the basis for potential sensing applications. Consistent with previous studies [79, 78], fluorescent colloids are adsorbed on defect positions, as shown in Fig 2.1c. This spontaneous positioning of colloids enables the accurate measurement of defect configurations, which could in turn be used for quantitative measurement of the concentration of particular substances in the vicinity of LC droplets.

To understand the driving force behind this structural transition, we introduce two

nanoparticles with no anchoring energy penalty at the interface of the ChLC droplet. Due to the affinity of nanoparticles to defects, the droplets are forced to adopt a TBS when two nanoparticles are positioned diametrically, even for high chirality. The elastic free energies of these resulting TBS droplets can be decomposed into splay, twist and bend free energies (details in Supporting Information). Fig 2.2e shows the dependence of each elastic energy contribution as a function of chirality (N). For $N = 0$, the splay elastic free energy dominates the bipolar structure for non-chiral nematic droplets. When N increases, due to the formation of the TBS morphology, the splay free energy near the point defects decreases significantly. The twist free energy increases as a result of the geometrical frustration incurred by chiral ordering in a spherical geometry. The first maximum of the twist free energy occurs near $N = 1$, and the directors near the boundary lie almost on the $x - y$ plane (blue layers in Fig 2.2a). This horizontal layer contributes to the increase of the bend energy. For N between 1.5 and 3.5, the bend free energy remains almost unchanged, while the twist free energy and the total free energy exhibit a minimum near $N = 2.5$. A second maximum in the twist free energy appears near $N = 3.75$, and is accompanied by the formation of the second horizontal layer, which comes with an increase in both the bend and splay free energies. The competition between three elastic free energies results in a minimum in the total elastic energy near $N = 2.5$. The formation of the TBS morphology does stabilize the system at low chirality, but when chirality increases beyond $N = 2.5$, the TBS droplet becomes less energetically favorable.

Additional insights can be gained when we consider different particle positions in the droplet with $N = 3.5$. The angle between the two lines connecting the nanoparticle centers and the droplet center is defined as α. As α decreases from 180°, the TBS transforms into a bent structure. The director fields for $\alpha = 180°, 140°, 100°$ and 60° are shown in Fig 2.3. These structures indicate that two surface point defects are absorbed by the nanoparticles, and the director field bends in a similar manner to that observed when θ decreases in the absence of nanoparticles. An analysis of the splay, twist and bend free energies for different α

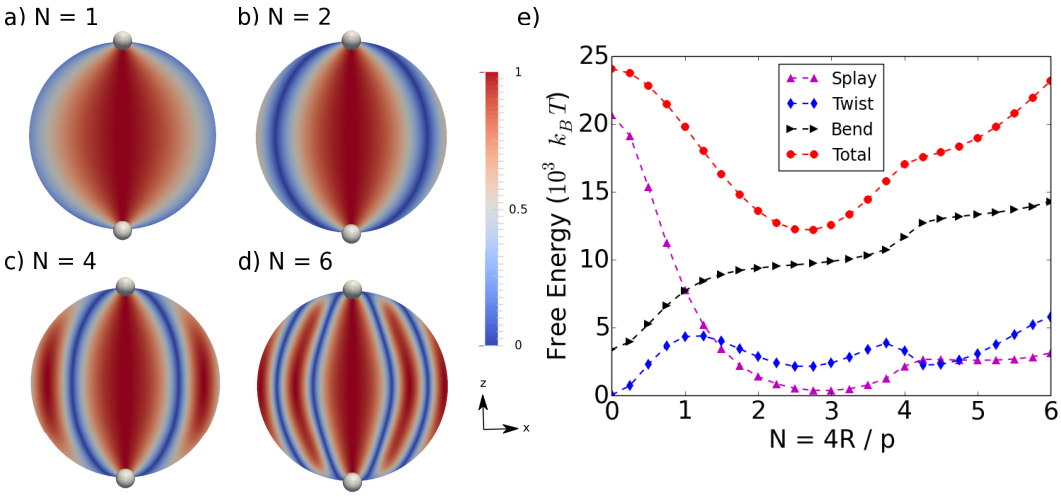

Figure 2.2: ChLC droplets ($W = 2.5 \times 10^{-3}\,\mathrm{J/m^2}$) with two nanoparticles ($W_{\mathrm{part}} = 0$) at the interface with antipodal positions. The director fields are colored by their projections onto the z-axis. a) - d) correspond to droplet director fields for increasing N. e) The graph shows the dependence of elastic energies as a function of N. The total elastic free energy finds its minimum near $N = 2.5$.

shows that the main contributions to the free energy come from bend and twist deformations. As α decreases from 180°, the bend distortion contribution increases, and in between the twist distortion contribution decreases. The balance between the bend and twist deformations leads to a minimum of total free energy at $\alpha = 126°$. It is close to $\theta = 139.7°$ in the pure droplet ($N = 3.5$). The slight difference could be due to the reduction of defect regions by the nanoparticles. Generally, for all values of chirality, as α decreases, the bend free energy increases and the twist free energy decreases. These results further emphasize that the formation of the bent structure is due to the competition between elasticity and chirality.

2.3.2 Structural Transition Induced by Anchoring Strength

As mentioned earlier, we are also interested in the effect of anchoring strength on the structure of ChLC droplets. Since for high chirality the droplets can get easily trapped in metastable states, we focus on intermediate values of chirality ($N = 3.5$).

For weak anchoring ($W \sim 10^{-7} - 10^{-6}\,\mathrm{J/m^2}$), elasticity and chirality dominate the free energy of the droplets. The stable state has a structure similar to the helical phase in the

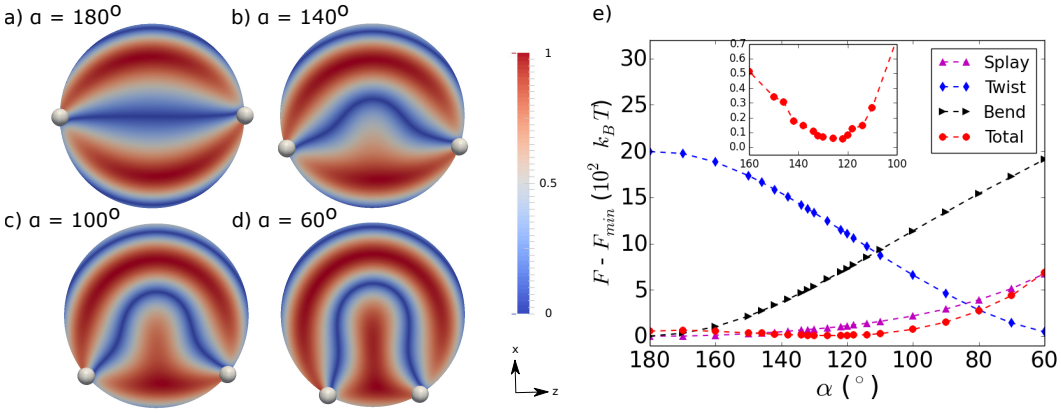

Figure 2.3: ChLC droplets ($N = 3.5$ and $W = 2.5 \times 10^{-3}$ J/m^2) with two nanoparticles ($W_{\text{part}} = 0$) at the interface with fixed positions. The angle between the two lines connecting the nanoparticle centers and the droplet center is defined as α. a) through d) are director fields corresponding to $\alpha = 180°, 140°, 100°, 60°$ respectively. The director fields are colored by their projections onto the y-axis. e) The graph shows the dependence of elastic energies as a function of α. As α increases, the director field bends more, causing the increase of bend distortion contribution. While the twist distortion contribution, which represents the chirality of the system, decreases. The inset graph shows that the total elastic energy has a minimum energy around $\alpha = 126°$.

bulk (Fig 2.4a) and the cholesteric layers are slightly bent. As shown in Fig 2.4g, in the region $W < 10^{-5}$ J/m^2, the elastic free energy remains small, while the surface free energy dominates the behavior of the droplets. As W increases, the surface free energy increases, because the energy penalty of the off-plane directors rises.

As W increases to 10^{-5} J/m^2, the surface energy reaches a maximum. The directors near the surface are forced to deform, in order to reduce the surface free energy. This deformation inevitably increases the elastic energy. The quasi-helical structure seen for weak anchoring evolves into a new structure, as shown in Fig 2.4b. This structure, obtained from a random initial configuration, is similar to the planar bipolar structure (PBS) proposed in previous numerical work [60]. Within one cholesteric layer (the y-z cross section in Fig 2.4e), the directors are mostly uniform except for those near the interface. On the x-y cross section (Fig 2.4f), different layers bend near the droplet surface and form a rounded rectangle structure.

Further increases of W lead to a sudden transition, at $W_{trans} \sim 5 \times 10^{-5}$ J/m^2. The PBS structure changes to the bent structure (Fig 2.4c). As W increases ($10^{-5} \sim 10^{-3}$ J/m^2), θ

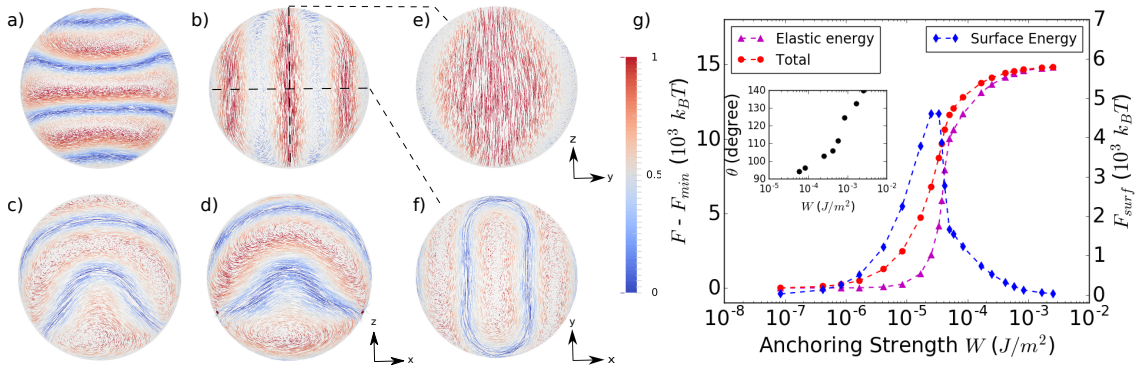

Figure 2.4: Director fields of ChLC droplets for $N = 3.5$ with anchoring strength (a) 4.2×10^{-6} J/m^2, (b) 4.2×10^{-5} J/m^2, (c) 5.0×10^{-5} J/m^2 and (d) 2.5×10^{-3} J/m^2. For a), c) and d), the director field is colored according to its projection onto the y-axis and for b) the director field is colored according to its projection onto the z-axis. e) and f) Director fields on the two cross sections of y-z plane and x-y plane for b) with $W = 4.2 \times 10^{-5}$ J/m^2. e) The director field shows that inside one cholesteric layer, the director is almost uniform in the central part and deforms near droplet surface. g) The dependence of elastic energy (contribution of both elasticity and chirality), surface energy and total free energy as a function of anchoring strength. The inset graph shows that for the bent structures with W above 5.0×10^{-5} J/m^2, θ increases as W increases.

varies continuously from 94.1° to 139.7° (Fig 2.4g). This structural transformation probably results from the competition between elasticity, chirality and surface energy. When the anchoring is strong ($W \gg W_{trans}$), the directors on the surface are almost tangential and the surface free energy is nearly zero. Meanwhile, the elastic free energy saturates to a maximum. In the end, we recover the bent structure for $N = 3.5$ with $W = 2.5 \times 10^{-3}$ J/m^2.

It is important to emphasize that the Kleman-de Gennes length [21] near the transition is around $0.84R$. Therefore, the transition occurs when the anchoring becomes non-negligible, in agreement with a Kleman-de Gennes analysis. Moreover, previous studies have stated that for the range of chirality ($1 \leq N \leq 14$), the PBS is always metastable in ChLC droplets with strong planar anchoring. In contrast, our results show that for $N = 3.5$, a narrow window of anchoring strength exists ($W \sim 4.2 \times 10^{-5}$ to 5.0×10^{-5} J/m^2) where PBS is energetically favorable and thermodynamically stable.

It is of interest to place our findings for chiral droplets in the context of results for purely nematic, achiral droplets ($N = 0$). For achiral drops one finds two stable morphologies: a

uniform configuration for weak anchoring ($W \sim 10^{-7} - 10^{-6}\,\mathrm{J/m^2}$), and a bipolar configuration for strong anchoring ($W \sim 10^{-4} - 10^{-3}\,\mathrm{J/m^2}$). The transition from a uniform to a bipolar state occurs over a board range of anchoring, *i.e.* W from 10^{-6} to $10^{-4}\,\mathrm{J/m^2}$ (Fig S1). In contrast, for chiral droplets the transition occurs over a much narrower range of W, between $4.2 \times 10^{-5}\,\mathrm{J/m^2}$ to $5.0 \times 10^{-5}\,\mathrm{J/m^2}$, indicating that the configurational transition of a ChLC droplet is much sharper than that of nematic LC droplet of comparable dimensions. Here we also note that, compared to the simple transformation (from bipolar to uniform) undergone by nematic LC droplets in response to anchoring, ChLC droplets can be engineered to exhibit a three-stage transition, from a helical structure (Fig 2.4a) to PBS (Fig 2.4b), from PBS to a bent structure (Fig 2.4c), and then an increase of θ in the bent structures (Fig 2.4d and Fig 2.4g). This richer response to interfacial cues may offer increased opportunities for development of multiresponsive materials based on ChLC droplets for applications in detection of molecular adsorbates.

2.3.3 Internal Structure of Radial Spherical Structure

In order to investigate the internal structure of RSS, we simulated a ChLC droplet of high chirality ($N = 16$) with the aid of ansatz (1.48). Fig 2.5b shows the periodic variation of the directors along the diametric direction within a RSS droplet ($R = 2\,\mu\mathrm{m}$). Here we define the mean period (p_m) as the average distance between every second feature, or between every other peak of director variations in y or z-axis in Fig 2.5b. The value of p_m can be used as a measure of p under the spherical confinement. As shown in Fig 2.5c, the relative change of period with respect to the intrinsic cholesteric pitch near the center $\frac{p_m - p}{p} = 0.45$ at $|x/R| \leq 0.18$) is much higher than that near the surface $\frac{p_m - p}{p} = 0.03$ at $|x/R| \geq 0.18$), given that $p/R = 4/N = 0.25$. It indicates that the value of p_m is much larger than p near droplet center but close to p near the boundary. As illustrated by the splay bend order iso-surface in Fig 2.5a, the twisting features near the CLC droplet center suffer from a considerable amount of bend elastic distortion. As a result, the twisting features near the droplet center

expand due to a delicate interplay between the elasticity, chirality, and anchoring, leading to a local increase of the period near the center of droplet and thus to an increase of the average period, p_m [68].

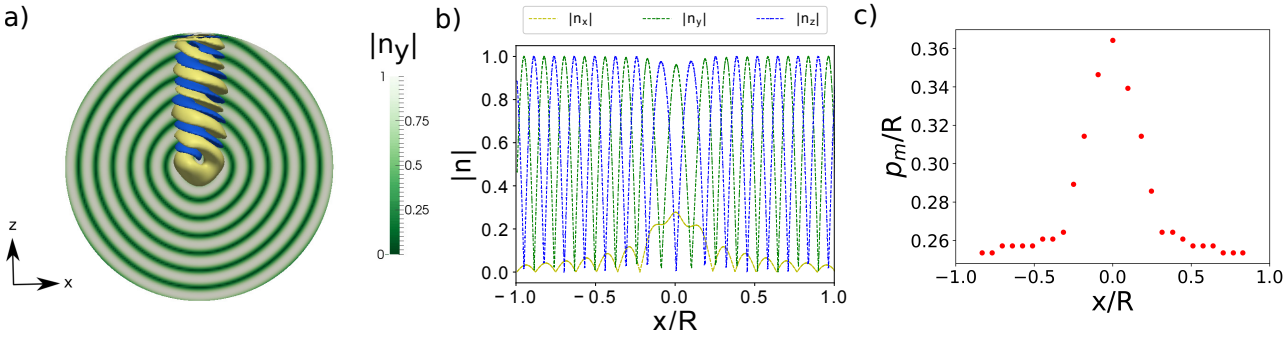

Figure 2.5: Results of simulations of cholesteric droplets. (a) The xz cross-section of a CLC droplet for $R = 2\,\mu$m and $N = 16$. The director field is colored according to its projection on the y-axis. The splay and bend distortions are shown in blue ($S_{\mathrm{SB}} > 0.0014$) and yellow ($S_{\mathrm{SB}} < 0.0014$), respectively. b) The variations of the directors x, y, z-components along the diametrical direction in x-axis. (c) The evolution of local average period p_m, estimated by maxima and minima of directors y component along the diametrical direction in the x-axis. The value of $p/R = 4/N = 0.25$.

2.3.4 Configuration Distribution of ChLC droplets

We measured the frequency with which we observed each of the above-described droplet configurations in experiments, as a function of N (Fig 2.6) [4]. We observed that for $N < 4$, 96% of LC droplets adopt the TBS. At intermediate N ($4 < N < 8$), the DSS and RSS were observed, but TBS was rare. For large N ($N > 8$), the RSS was the most frequently observed configuration reaching 99% of the droplets for $N > 16$. These observations coincided well with simulation results that predict the TBS to be the most stable structure for small N ($N < 3$) and RSS to be the most stable structure for large N ($N > 3$). For N between 3 and 4, we observed the distance separating the two surface defects to decrease with increase in N, leading to a continuous change from TBS at $N = 3$ to RSS at $N = 4$. The simulation result of meta-stable DSS configuration is obtained from Ansatz (1.48).

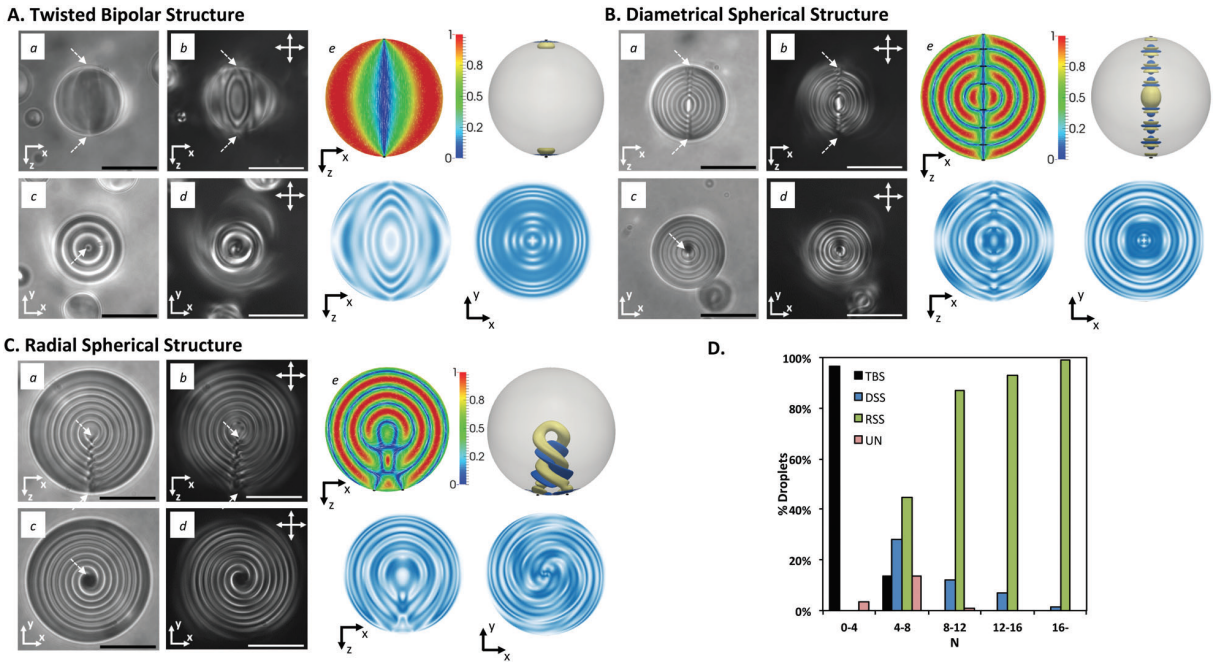

Figure 2.6: (A-C) Optical micrographs of the three most commonly observed configurations of cholesteric LC droplets: (A) Twisted bipolar structure (TBS), (B) Diametrical Spherical Structure (DSS), and (C) Radial Spherical Structure (RSS). The white double-headed arrows indicate the orientation of the crossed polarizers, single headed solid arrows indicate the imaging planes, and dashed arrows show the location of LC defects. Scale bars: 20μm. (D) Percentages of cholesteric LC droplet configurations with respect to N. TBS: Twisted bipolar structure, DSS: Diametrical Spherical Structure, RSS: Radial Spherical Structure, and UN: Unidentified structure. The histograms were assembled from 913 droplets in 13 independent experiments.

2.3.5 Quenching Process from Isotropic to Nematic Phase

Note that by starting from a random initial configuration, we are also able to reproduce the fast quenching process that is employed in experiments. The first row in Fig 2.7 shows a series of optical micrographs obtained from a 2.5 wt% S-811 in 5CB droplet dispersed in water following a fast thermal quench from the isotropic phase to the cholesteric phase. The numerical results for the dynamics of morphology formation of RSS during quenching are displayed below, and found to be in good agreement with our experimental observations. Initially, order is only obtained locally, and disclination lines span the entire droplet. As time proceeds, the ordered region continues to expand, accompanied by the annihilation of defects. At a certain point, twisting layers emerge in one hemisphere of the droplet, and all

disclination lines are squeezed onto the other end. This process is followed by the shrinkage of the disordered regions. As quenching concludes, the RSS is fully formed, and has only two defect points on the surface.

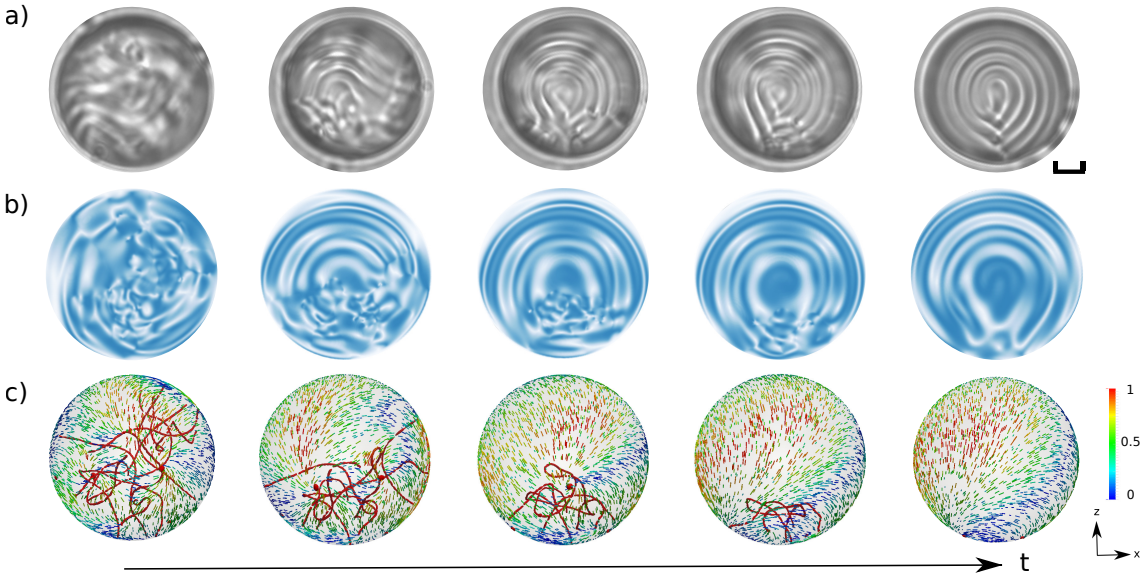

Figure 2.7: Time sequence of the quenching process for chiral droplets, from the isotropic phase to the RSS morphology. Three rows correspond to a) series of experimental micrographs of 2.5 wt% S-811 in 5CB droplets dispersed in water that is thermally quenched from the isotropic phase (50°C) to the cholesteric phase at room temperature (scalar bar: 5 μm), b) simulated polarization graphs and, c) director field on the surface and scalar order parameter iso-surfaces (in red). The director field is colored according to its projection onto the z-axis.

CHAPTER 3

CHOLESTERIC NEMATIC SHELLS

3.1 Introduction

Previous chapter exhibits a variety of intriguing twisted mesophases in ChLC droplets and its potential use as stimuli-responsive materials. To broaden the spectrum of defect textures, this chapter examines the nematic shells, which denotes liquid crystals confined within two spherical surfaces.

In 1992, Lubensky and Prost predicted a spherical vesicle structure with four disclination lines at the vertices of a tetrahedron [33], in contrast to configurations found in droplets or channels. Later, Nelson proposed the creation of nematic shells coated with colloids functionalized as to provide a 4-fold valence, resembling sp^3 hybridized chemical bonds [44]. Using double-emulsion techniques, experiments were able to identify not only tetravalent structures, but also bivalent and trivalent LC shells with interfacial parallel orientations (planar anchoring) [11, 29, 22]. Through addition of surfactants, the anchoring type of either the inner or the outer surface of a shell can be tuned, leading to possible control over distinct structures [28, 27, 26]. Numerical studies have also sought to investigate the role of shell geometry, elastic anisotropy and thermodynamic conditions on defect configurations using Ginzburg–Laudau minimizations and Monte Carlo methods [76, 65, 59, 64, 77]. Recent work reported results for shells with embedded micro-particles and examined the configurations resulting from interactions between topological defects and micro-particles [14].

In this chapter, we consider two questions that, to our knowledge, have only been partially addressed. The first is, what configurations will the helical structure adopt when confined in shells? Second, we ask whether that chiral order can be manipulated and, if so, what are the resulting defect structures? To do so, we rely on a Landau–de Gennes (LdG) continuum model that enables systematic study of micrometer-sized nematic shells with strong parallel anchoring (degenerate planar anchoring) on both surfaces. We begin by validating our

methods by comparing predictions for non-chiral nematic LC shells to available experiments. We then introduce chirality in uniform shells and examine the effects of thickness. Our results reveal the existence of a tetravalent structure, a bipolar structure, a bent structure and radial spherical structure (RSS). To characterize the phase boundaries between these structures, we introduce the shell chirality c as an order parameter; it is given by the ratio of shell thickness to pitch. Importantly, in uniform shells, the transition from bipolar structure (BS) to RSS occurs in a narrow window of both chirality and shell geometry, implying that shells could provide a sharp response to external stimuli. We also investigate the role of elastic forces on the inner drop for intermediate and high values of chirality, and find that asymmetric stable configurations are highly dependent on shell chirality c [83].

3.2 Model and Methods

3.2.1 Simulation details

The numerical parameters employed here are used: $A = 1.17 \times 10^5\,\mathrm{J/m^3}$, $U = 5$, $L = 6 \times 10^{-12}$ N, $W = 10^{-3}\ \mathrm{J/m^2}$, the radius of outer sphere is $R = 1\,\mu$m. The equilibrium value of the nematic order parameter S_{eq} is therefore 0.762. Different initial conditions are used, including random configurations, uniform configurations and radial spherical configurations (1.48).

3.2.2 Experiment details

In our experiments, LC shells were produced using a glass capillary microfluidic device, based on the design developed by Utada and his coworkers. [75] The LC 4'-pentyl-4-cyanobiphenyl (5CB, Sigma Aldrich) is co-injected with an inner aqueous phase and flow-focused by an outer aqueous phase, producing spherical shells of 5CB that encase the inner fluid and are suspended within the outer fluid. Both inner and outer aqueous phases consist of 5 wt.% polyvinyl alcohol (PVA, MW: 13,000-23,000, 87-89% hydrolyzed, Sigma Aldrich), which pro-

motes planar anchoring on both shell surfaces. Shells are collected in a petri dish containing a bath of 5 wt.% PVA before observation using a polarized-light microscope (Olympus BX51).

3.3 Results and Discussion

3.3.1 Non-chiral Nematic Shells

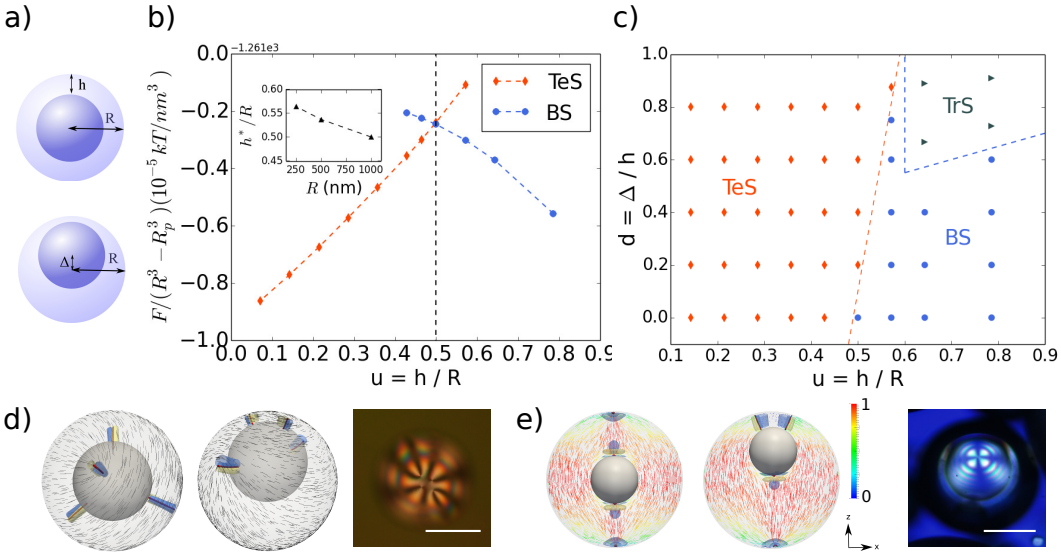

Figure 3.1: a) Schematic diagrams for h, R and Δ. b) Free-energy density graph as a function of u for bipolar structure (BS) and tetravalent structure (TeS). The cross-over of two curves demonstrates BS-to-TeS transition at $u^* \simeq 0.5$. The inset graph shows the dependence of transition thickness u^* on the droplet radius R. c) d-u phase diagram for non-chiral nematic shell. Red diamond, blue circle and black triangular correspond to TeS, BS and trigonal structure (TrS). d) Left and middle: simulation results of tetravalent structures (TeS) with $u = 0.429$ (left: $d = 0$, middle: $d = 0.667$). Director fields on the outer surface are shown in black lines. Right: cross-polarized light image of TeS configuration observed in experiments. Scale bar: $200\,\mu$m. e) Left and middle: bipolar structures (BS) with $u = 0.643$ (left: $d = 0$, middle: $d = 0.667$). The director fields are on x-z plane, colored by the projection to z-axis. Right: cross-polarized light image of BS configuration. Scale bar: $100\,\mu$m. For both d) and e), the defects are shown in red (isosurface for $S = 0.5$ with $S_{eq} = 0.762$); the splay and bend elastic distortions are shown in blue ($S_{\mathrm{SB}} > 0.002$) and in yellow ($S_{\mathrm{SB}} < -0.002$), respectively.

To validate our calculations, we briefly consider non-chiral nematic shells. We investigate concentric (symmetric or uniform) nematic shells with different shell thickness $h = R - R_p$, where R_p is the radius of the inner drop (Fig. 3.1a). For convenience, we introduce a dimen-

sionless parameter $u = h/R$ to describe thickness, ranging from 0 to 1. In agreement with experimental observations [11] and past theoretical work [64, 76], two different configurations are observed: a bipolar structure (BS) with two ($s = +1$) antipodal point defects, and a tetravalent structure (TeS) with four ($s = +1/2$) disclination lines. Both structures have a total topological charge of ($s = +2$) on the outer surface, as required by the Poincare-Hopf theorem [51]. Fig. 3.1b shows that BS and TeS are stable configurations for thicker shells ($h \geq R/2$) and for thinner shells ($h \leq R/2$), respectively. The critical thickness of this BS-to-TeS transition u^* is 0.5, same as that observed in experiments [11]. As illustrated in the inset of Fig. 3.1b, u^* depends on shell size R (or curvature $1/R$). Note that a larger value of $u^* = 0.666$ was reported in previous work [64]; we attribute the difference to the small (and more relevant) shell sizes considered here ($R \sim 100$ nm); indeed, our micrometer-sized simulations yield results in quantitative agreement with experiment.

Due to buoyancy effects (arising from the mismatch of density) and elastic forces induced by the liquid crystal, the inner drop may not remain in the center of the large drop. We therefore also consider briefly the role of elasticity in producing eccentric (asymmetric or inhomgeneous) shell configurations. As illustrated in Fig. 3.1a, the displacement Δ is defined as the distance between the inner and outer drop centers. We also define the degree of asymmetry as $d = \Delta/h$, which varies from 0 to 1: $d = 0$ corresponds to a uniform shell and $d = 1$ corresponds to a shell configuration in which the inner drop touches the outer drop surface. Fig. 3.1c depicts the d-u phase diagram, consisting of three major phases: a tetravalent structure (TeS), a bipolar structure (BS), and a trigonal structure (TrS). For thin shells, as eccentricity increases (Fig. 3.1d), the four disclination lines in TeS move towards the thinner layer of the shell. The trajectory and configurations for this TeS deformation in asymmetric shells have been studied in previous work [59]. As for thicker shells, when d becomes large (generally $d \geq 0.6$), BS transforms into a trigonal structure (TrS) with two ($s = +1/2$) disclination lines and a pair of point defects ($s = +1$), as shown in Fig. 3.1e. In order to support our calculations, we performed experiments with 5CB to fabricate both

thin and thick nematic shells with parallel anchoring (Fig. 3.1d and 3.1e). The agreement between simulation and experiments serves to demonstrate that the model adopted here can capture key features of nematic shells. To conclude, for the entire range of u considered here, the free energies are minimized when the inner drop approaches the outer drop periphery (d reaches 1), in agreement with our observations and also with past experimental and simulation reports [11, 59, 64].

3.3.2 Concentric Chiral Nematic Shells

Previous studies of chiral nematic droplets have revealed that, when confined in a spherical geometry, nematic materials adopt new configurations, such as the twist bipolar structure and RSS. Such structures are considerably different from the helical phase observed in the bulk [1, 60, 80]. When a chiral nematic is bounded between two spherical surfaces, in shells, we anticipate that more configurations will arise.

To investigate the effect of chirality on shells, we first consider high chirality concentric shells ($\Delta = 0$ and $N = 4R/p = 8$) of varying thickness u (as shown in Fig. 3.2b). In analogy to non-chiral nematic shells, a phase transition from TeS to twisted bipolar structure (BS) occurs as the shell thickness (u) increases. Note that we use BS as the abbreviation for both (non-chiral) bipolar structures and (chiral) twisted bipolar structures. In highly chiral systems, we observe a second transition from BS to a radial spherical structure (RSS) shell when u reaches 0.43, and into an RSS droplet in the limit of $u = 1$. The RSS shell has concentric cholesteric layers with two surface point defects on the outer and inner surfaces, respectively. The two cholesteric λ^{+1} disclination lines, shown in yellow in Fig. 3.2b ($u = 0.43$), start from the inner surface defects, and then span the shell in a helical manner until they reach the outer surface defects. [60]

As discussed in the preceding section, the non-chiral nematic shell ($N = 0$) with $u = 0.43$ exhibits a tetravalent structure (TeS). We therefore examine how, in a shell with $u = 0.43$, does TeS ($N = 0$) transform into RSS ($N = 8$) as chirality increases. Figure 3.2a shows

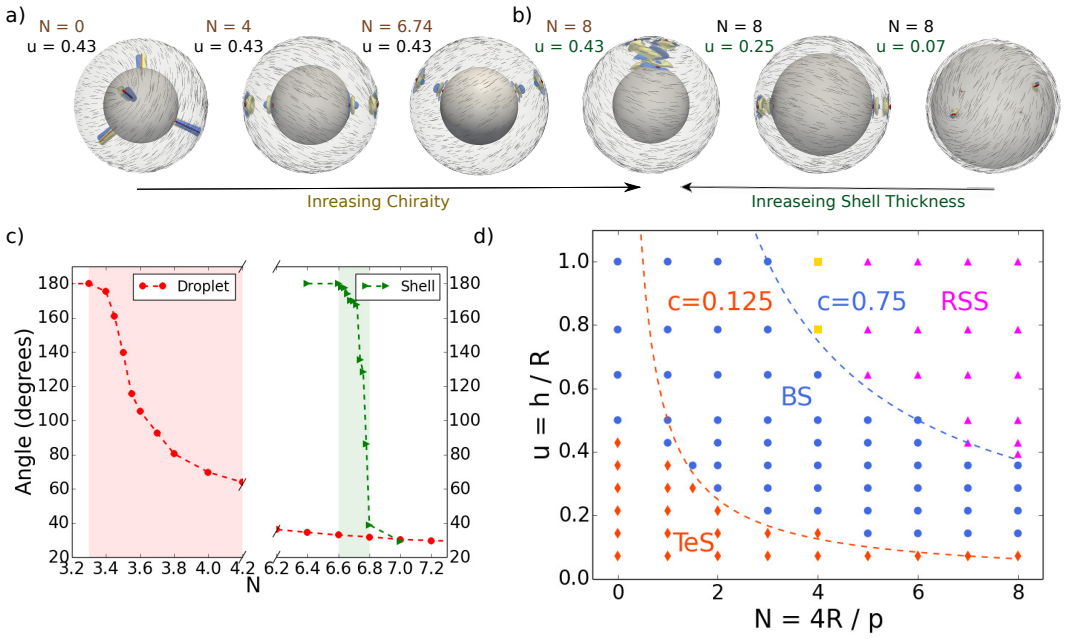

Figure 3.2: a) and b) Shell configurations (from left to right: TeS, BS, Bent structure, RSS, BS and TeS) with different chiralities ($N = 4R/p$) and shell thicknesses ($u = h/R$). Director fields on the outer surface are shown in black lines. Defects are in red. The splay and bend elastic distortions are shown in blue ($S_{\rm SB} > 0.002$) and in yellow ($S_{\rm SB} < -0.002$), respectively. c) Graph of Θ as a function of N for droplet (red circle) and uniform shell with ($u = 0.43$) (green triangle). d) The u-N phase diagram for concentric shells. Red diamond, blue circle, yellow square and magenta triangle correspond to TeS, BS, bent structure (BeS) and RSS, respectively. $c = h/p = uN/4$ represents the shell chirality.

two structural transitions: a TeS-to-BS transition ($0 \leq N \leq 1$), followed by a BS-to-RSS transition ($6 \leq N \leq 7$) with the bent structure (BeS) as an intermediate configuration (Fig. 3.2a: $N = 6.74$). This BS-to-RSS transition, as well as the BeS structure in a chiral LC droplet, were studied in a recent publication from our group. [82] A comparison of BS-to-RSS transitions between these two distinct geometries is displayed in Fig. 3.2c. Here we define the angle between the two lines connecting outer surface point defects to the droplet or shell center as Θ. Thus, $\Theta = 180°$ for BS, $\Theta \sim 30°$ for RSS and Θ in between for BeS. We have recently reported on a drastic decrease of Θ in chiral LC droplets within a narrow window of chirality ($3.3 \leq N \leq 4$), which correspond to a continuous transition from BS to RSS. Strikingly, this transition is even sharper in shells ($u = 0.43$), indicating a higher sensitivity of shell geometries to environmental disturbance (chirality) (and better

performance for potential uses in sensing).

A u-N phase diagram is shown in Fig. 3.2d. Three distinct phases are involved: TeS in thinner shells with low chirality, RSS in thicker shells with high chirality, and BS in between. Even though $N = 4R/p$ is commonly employed to describe chirality in droplets, it fails to characterize an extremely important parameter, thickness, in shells. This phase diagram suggests that an important parameter for shells is $c = h/p = uN/4$, which measures the ratio of shell thickness h to pitch p. Different from N, which quantifies the approximate number of π turns along the diametrical axis, c captures the number of 2π turns along the radial direction in a uniform shell. The two dotted curves ($c = 0.125$ and $c = 0.75$) in Fig. 3.2d define two phase transition boundaries. In concentric shell geometries, as shell chirality c increases, a TeS is initially the most stable configuration, followed by a BS, which finally transforms into RSS. Similarly to previous findings for chiral LC droplets in our group [82], these transitions are the result of an interplay between elasticity and chirality.

Note that the $c = 0.125$ curve deviates from the real phase boundary near $N = 0$. This is because when N is close to 0, shell chirality $c = uN/4$ becomes too small to reveal the effect of u (or h), thereby failing to characterize the phase boundary. Another issue for c is that it only takes into account the shell thickness h, but fails to quantify curvature ($1/R$). To illustrate the importance of curvature in a shell geometry, we recapitulate the dependence of the TeS-to-BS transition thickness u^* on curvature $1/R$ in Fig. 3.1b. In this work, we simply fix R. A more complex expression, consisting of R, Rp and p, could be proposed to provide a better order parameter in systems of varying size.

3.3.3 Inhomogeneous Chiral Nematic Shells

To the best of our knowledge, the role of elasticity on inner drop position in chiral nematic shells has been barely studied [77]. Here we consider two representative cases: intermediate chirality ($N = 4$) and high chirality ($N = 8$). Figure 3.3a shows the d-u phase diagram for chiral nematic shells with $N = 4$. It exhibits three essential differences from what is observed

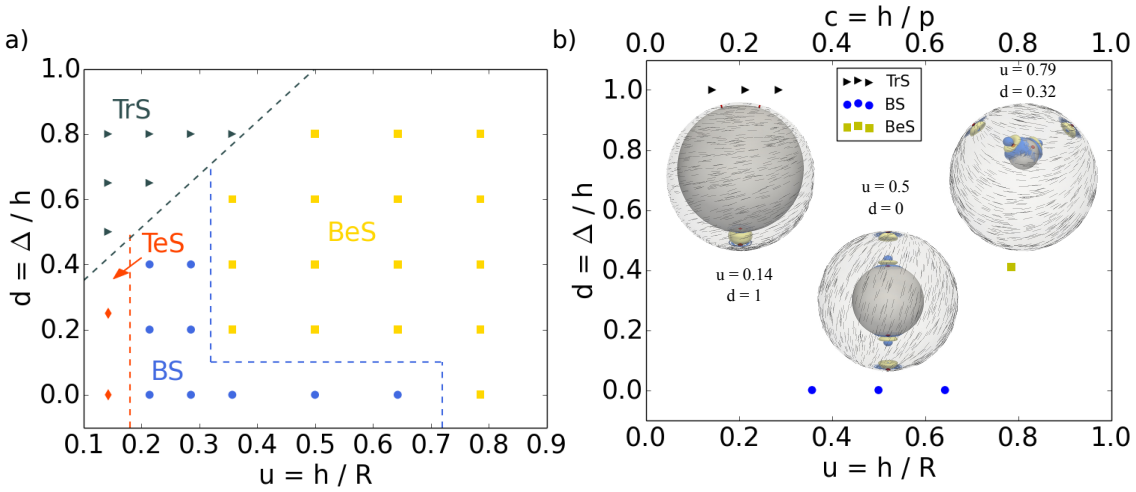

Figure 3.3: a) d-u phase diagram for chiral nematic shell ($N = 4$). Red diamond, blue circle, black triangle and yellow square correspond to TeS, BS, TrS and bent structure (BeS), respectively. b) Diagram of the relative energetically favorable position d for different shell thickness. Inset images are representative shell configurations for TrS ($u = 0.14$, $d = 1$), BS ($u = 0.5$, $d = 0$) and BeS ($u = 0.79$, $d = 0.32$). Director fields on the outer surface are shown in black lines. Defects are in red. The splay and bend elastic distortions are shown in blue ($S_{\mathrm{SB}} > 0.002$) and in yellow ($S_{\mathrm{SB}} < -0.002$), respectively.

for $N = 0$ d-u (as in Fig. 3.1c). First, the three phases (TeS, BS and TrS) in non-chiral shells ($N = 0$) shift to regions of small u in chiral shells ($N = 4$). Second, a new phase, a bent structure (BeS), appears in thicker shells and is greatly favored in inhomogeneous shells. Finally, in thin shells ($N = 4$), as d gets large, TeS is no longer as prevalent as it is in non-chiral shells ($N = 0$), and TrS takes over.

In constrast to non-chiral shells, where the inner drop always move towards the outer boundaries of the drop surface, chiral shells (N = 4) manifest a diversity of energetically favorable positions (d) for different shell thickness (u). Here, we offer an explanation based on shell chirality c. For thin shells, when c is small, similar to non-chiral systems ($c = 0$), the inner drop moves towards the outer drop periphery due to elasticity. As c nears 0.5, where the director follows a rotation of approximately π along the radial direction in uniform shells, the inner drop prefers to stay in the center. Thicker shells ($c \geq 0.75$) adopt configurations similar to those of chiral LC droplets. Because of higher splay and bend distortions on one side of the BeS or RSS droplets, the inner drop favors a slightly off-center position.

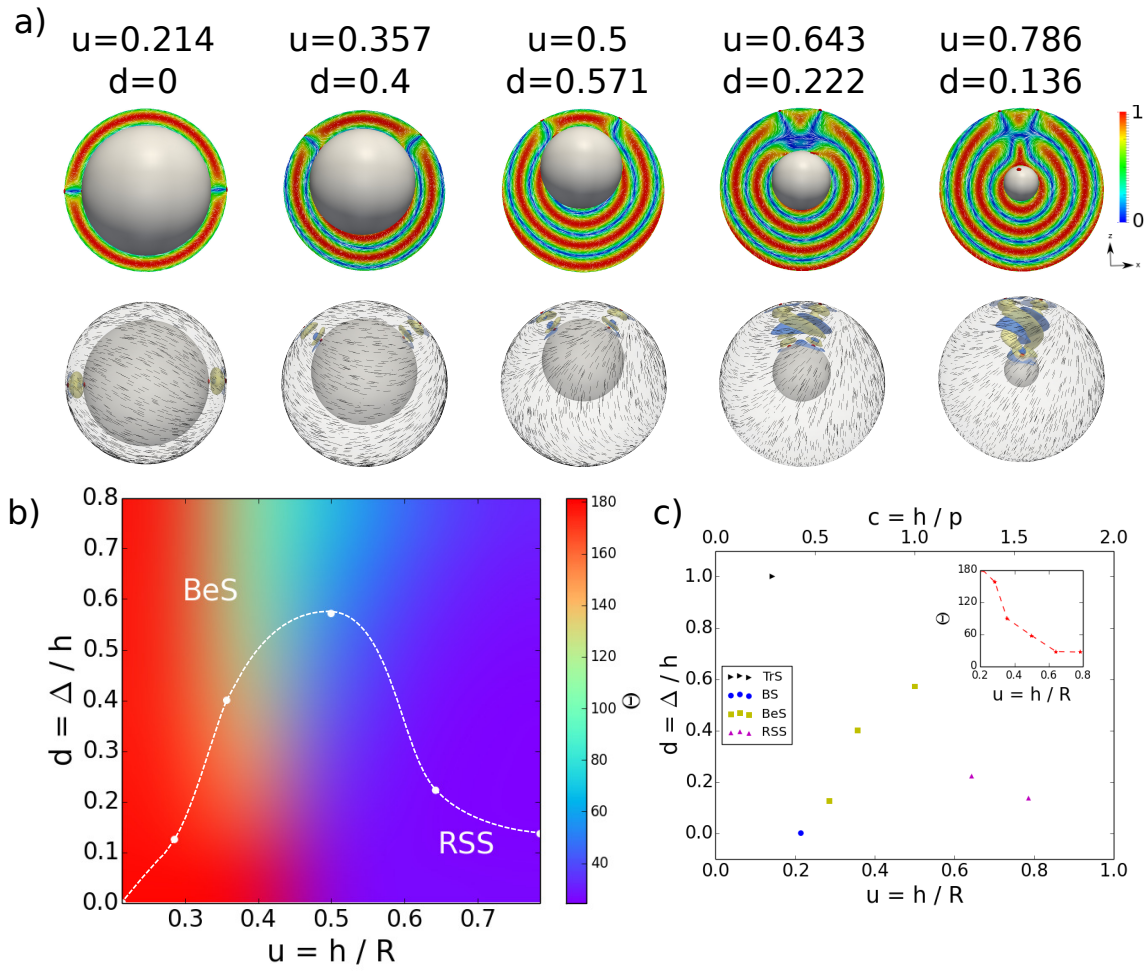

Figure 3.4: a) Representative shell configurations ($N = 8$) with minimum energies for varying thicknesses. In the first row, the director fields are on x-z plane, colored by the projection to y-axis. In the second row, director fields are on the outer surface, defects are in red and splay-bend elastic distortions are shown in blue ($S_{\mathrm{SB}} > 0.002$) and in yellow ($S_{\mathrm{SB}} < -0.002$). b) 2D map of Θ with different $d = \Delta/h$ and $u = h/R$. c) Diagram of energetically favorable positions d for different shell thickness with $N = 8$. Inset graph shows how Θ of corresponding configurations varies as u increases.

We close by examining the behavior of highly chiral shells ($N = 8$) in response to u and d. As shown in Fig. 3.4c, similarly to shells with $N = 4$, when shell chirality c is small, the inner drop moves towards the outer surface; when $c \sim 0.5$, the inner drop prefers to stay in the center; when c further increases, a bent structure appears and the inner drop adopts a slightly off-center position. A unique feature of highly chiral systems is that, when shell chirality is large ($c \geq 0.7$), shells adopt an RSS configuration. The small inner drops in RSS

shells prefer to stay near the center position, probably due to a competition between surface anchoring and elastic energy.

When $u \geq 0.214$, chiral shells ($N = 8$) consist of only BS ($\Theta = 180°$), BeS ($180° > \Theta > 30°$) and RSS ($\Theta \sim 30°$). One can therefore generate a 2D map of Θ as a function of d and u. For uniform shells ($d = 0$), the BS-to-RSS transition occurs within an extremely narrow range ($\Delta u \leq 0.007$). The sharp response to shell geometry resembles that to chirality, suggesting a potential use of chiral shells as sensors. Deformations of defect configurations occur as shell symmetry is broken. Generally speaking, the shell thickness inhomogeneity induces a decrease of Θ for BS shells and an increase of Θ for RSS shells. Interestingly, those minimum energy positions for varying shell thickness form a path with a continuous decrease of Θ from 180° to 30° (as shown in Fig. 3.4b), which corresponds to the BS-to-RSS transition. In experiments, the shell thickness u can be easily changed by inducing a difference in osmotic pressure between the inner and outer water phases through addition of salts [29]. The transformation path from BS to RSS in highly chiral shells (N = 8) predicted by our simulation (as shown in Fig. 3.4a) mimics what is seen in experiments [8]. The inset of Fig. 3.4c describes how Θ decreases as shell gets thicker. It demonstrates that when the restriction of a central inner drop is removed, the decrease of Θ from 180° to 30° becomes much slower ($\Delta u \sim 0.43$), compared with the sharp response to shell thickness observed in uniform shells ($\Delta u \leq 0.007$).

CHAPTER 4

REORIENTATION OF DEFECTS IN NEMATIC SHELLS UNDER EXTERNAL FIELDS

4.1 Introduction

The presence of topological defects determines a large extent of materials' physical properties. As a result, understanding their behavior is of essential importance in a variety of fields, such as quantum physics, magnetism and cosmology. Liquid crystal phases, which exhibit a myriad of defect configurations and textures, offer an excellent arena to study the physics of defects. The previous chapter demonstrates a broad spectrum of spontaneously occurring defect configurations manifested by nematic shells, including tetravalent configuration with four $+\frac{1}{2}$ defects. Based on this fact, Nelson proposed an approach to fabricate tetravalent colloids by coating spherical particles with anisotropic material and discussed the possibility of obtaining other valences. Recently, different methods have been reported to control the topological defects, such as the thickness (thickness gradient) [29], elastic constant [65, 59] and curvature [58], however neither of them are efficient in controlling defect numbers.

Since nematic LCs have a lager dielectric constant along the molecular long axis, the application of electric field to the shell leads to the alignment of the director $\mathbf{n}$ (Equation 1.35). In 2008, Skačej and Zanonni proposed a technique to control the defect number via external field [66]. They performed Monte Carlo (MC) simulations to study the structural transformation from the tetravalent shell to bipolar structure under a strong uniform field. Moreover, they reported the nucleation of more complicated defect patterns via inhomogeneous higher order multipole fields. Their simulation work indicates that the external fields can be an excellent tool to manipulated the defect number, strength and position. However, only typical cases were investigated, also the director configurations during the evolution and mechanisms remain unanswered.

In this chapter, we examined the effect of external fields on both homogeneous and inho-

mogeneous tetravalent nematic LC shells in both simulation and experiments. We observed the topological transformations stemming from the alignment of the director with the strong uniform magnetic field, which eventually lead to the formation of bipolar configurations, in agreement with the work by Skačej and Zanonni [66]. Beyond that, we found that the defect motions during the transformation depend on both the defect orientations and external field directions. By examining elastic distortions with the aid of splay-bend order parameter (1.22) during evolution, we have shown that the defect motions is closely related the formation of disclination walls (1.6).

4.2 Model and methods

4.2.1 Simulation details

The numerical parameters used in this work are $A = 1.067 \times 10^5$ J/m^3, $U = 5, L = 6$ pN, $W = 1 \times 10^{-3}$ J/m^2, $\hat{B} = 0.1$. The shells have outer radius $R = 1\,\mu$m. For homogenous shells, inner radius $R_p = 786$ nm. For the inhomogeneous shells, inner radius $R_p = 643$ nm and the displacement is $d = 257$ nm.

4.2.2 Experiment details

The shells are produced by conventional double emulsion method in a grass capillary microfluidic device [75]. The middle phase is 4-n-pentyl-4-cyanobiphenil (5CB), a liquid crystal with nematic phase at room temperature. The inner and outer liquids are aqueous solutions containing 1 wt% of polyvinyl alcohol (PVA), which stabilizes the double emulsion and enforces planar anchoring of the liquid crystal at the inner and outer interfaces. The experimental shells are inhomogeneous in thickness due to buoyancy effect and nematic elasticity. Typical size of the shells are $100 - 200\,\mu$m in diameter. The shell thickness is about several micrometers. To obtain homogeneous shells we use a swelling process to produce super thin shells ($< 1\,\mu$m), which leads to the regular tetrahedron defect structure [29].

Fabricated shells were collected by a 1 mm inner diameter square capillary, and the set on the sample holder was made using a 3D printer. A couple of permanent neodymium magnets were set face to face and the capillary were placed between the magnets, which enable us to apply a strong ($\approx$ 0.5 T) and uniform magnetic field in perpendicular to the gravity direction. To apply the magnetic field parallel to the gravity direction, we use hollow cylinder shape neodymium magnet and places the shell inside the hole which also induce strong ($\approx$ 0.5 T) uniform field. All experiments are performed at room temperature.

4.3 Results and Discussions

4.3.1 Homogeneous Nematic Shells

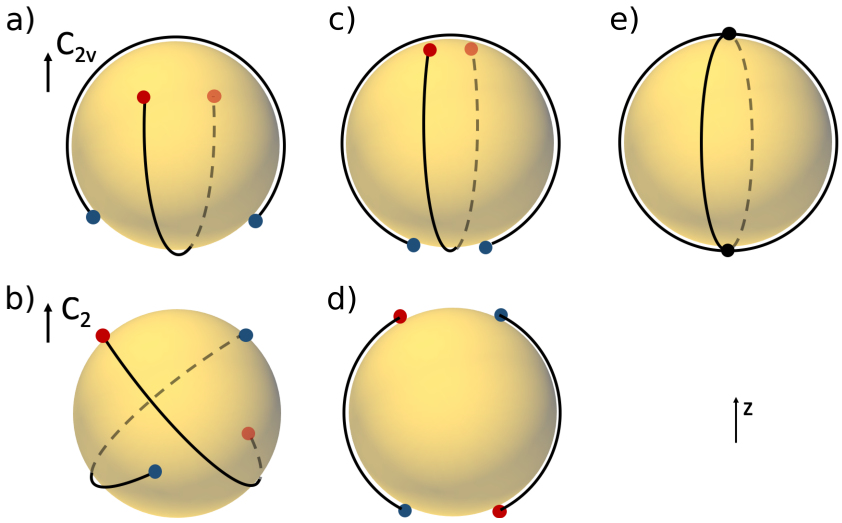

Figure 4.1: Schematic representation of homogeneous tetravalent shells with two pairs of defects shown in blue and red circles. Each pair is connected by the director streamline in black. a) Homogeneous nematic shell with no external field and C_{2v} axis parallel to z-axis. b) Same configuration as a) but with C_2 axis parallel to z-axis. c-d) Intermediate shell configuration during evolution upon the application of strong uniform external field along z-axis, C_{2v} and C_2 axis respectively. e) Final equilibrium bipolar configuration with strong uniform external field applied along z-axis.

The defect configurations of homogeneous thin nematic LC shells possess four $+\frac{1}{2}$ defects, the positions of which exhibit a tetrahedral symmetry including three C_{2v} axes. The C_{2v}

axis includes a two-fold rotational symmetric axis (C_2) and two orthogonal mirror planes containing the C_2 axis. However, the existence of director fields breaks the degeneracy of these four defects. As a result, only one of the C_{2v} axis (Fig 4.1a) maintains its symmetry, and the other two degrade to a lower-order-symmetry, C_2 (Fig 4.1b). To better illustrate it, we group the defect to two pairs based on their connections by director streamlines, as shown in Fig 4.1 as red and blue circles. These two pairs of defects are called as red pair and blue pair in the following text, for the purpose of simplicity.

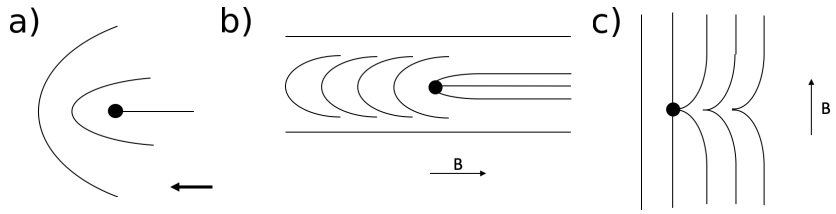

Figure 4.2: a) Director orientation of $+\frac{1}{2}$ defect, denoted by the arrow. b-c) Planar solitons produced by a field parallel and perpendicular to the $+\frac{1}{2}$ defect orientation. In both cases, Helfrich walls appear, with one parallel to B (b) and the other perpendicular to B (c).

Before diving in, we first take a glance at the possible structural transformation of single $+\frac{1}{2}$ defect (Fig 4.2a) induced by the external field (B). Here, we denote the defect orientation as the direction pointed by the arrow in Fig 4.2a. When B is applied parallel to the defect roientation, a bend-splay Helfrich wall (Fig 1.6b) appear in the defect orientation direction, as shown in Fig 4.2b. While if the relative orientation is perpendicular, it forms a splay-bend Helfrich wall (Fig 1.6c)instead and it is perpendicular to B. They have been referred to as planar solitons [5] and in these chapter we will name them as bend wall and splay wall, respectively.

In order to understand the effect of external fields on the defect configurations, we apply a strong uniform magnetic field along the C_{2v} and C_2 axes of nematic shells and monitor the resulting defect motions.

When the external field B is along C_{2v} axis, its projection on the surface (B_s) at the defect position is parallel to the defect orientation, resulting in the formation of bend walls (Fig 4.2b) in pairs. Fig 4.3e shows one of these pairs connected by a disclination wall with major

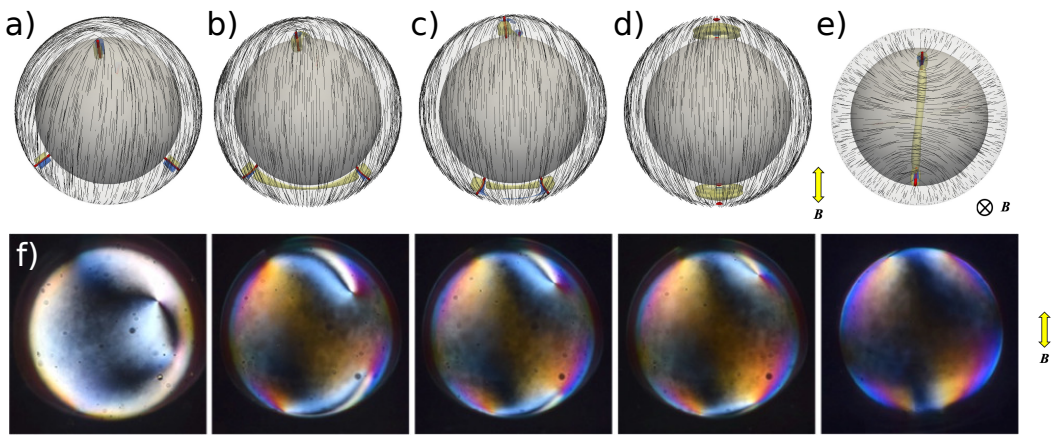

Figure 4.3: Reorientation of an homogeneous nematic shell under uniform magnetic field along C_{2v} axis. a-d) The director fields on the outer surface at 0, 3000, 13000, 44000 iteration steps. The defects are shown in red (isosurface for $S = 0.5$); the splay and bend elastic distortions are shown in blue ($S_{\mathrm{SB}} > 0.005$) and in yellow ($S_{\mathrm{SB}} < -0.005$), respectively. e) Top view of the director field and the bend-splay Helfrich wall of b). f) Experimental observations of defect motions upon the application of magnetic field with initial tetrahedron shell focusing on a upper right $+\frac{1}{2}$ defect.

bend distortions in yellow. Since the disclination wall bears high elastic energy, it shrinks and leads to the defects approaching each other in pairs until the final coalesencence to a +1 defect. The complete transformation is shown in Fig 4.3 a-d, where Fig 4.3d illustrates the final bipolar configuration. A schematic representaion of the intermediate state is provided in Fig 4.1c. Our numerical calculations recover the possiblity of controling valence number via external fields, which is in agreement with the previous MC simulation report [66] and are further confirmed by our experimental observations as shown in Fig 4.3f.

When the external field is applied parallel to the C_2 axis (Fig 4.1b), we observed an unexpected rotation of defects. To better understand this unnatural behavior, we plot the director fields of nematic shells during the evolution in Fig 4.4 with both side view (a-d) and top view (e-h). In this case, the initial defect orientations are no longer parallel to B_s. As a result, the bend walls are along the defect orientation near the defect, but continuously wind itself be aligned with B_s and connect with the other soliton. It leads to the formation of an S-shape bend wall (Fig 4.4f). As a consequence, the defects move along the curved disclination walls to reorient their defect orientations to be parallel to B_s (Fig 4.4g) until

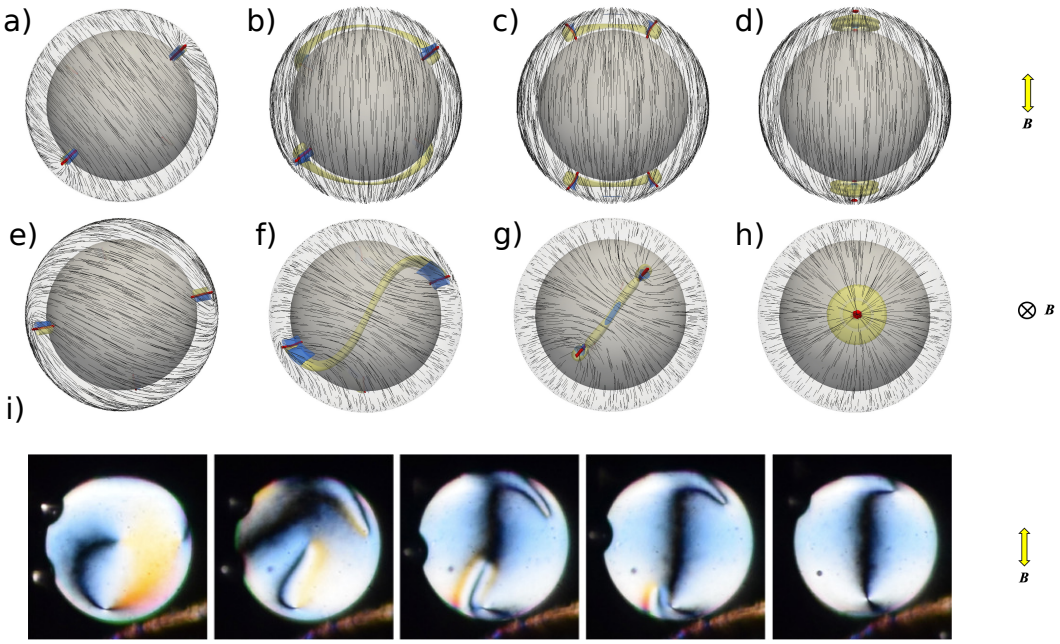

Figure 4.4: Reorientation of an homogeneous nematic shell under uniform magnetic field along C_2 axis. a-d) The director fields on the outer surface at 0, 3000, 13000, 44000 iteration steps. The defects are shown in red (isosurface for $S = 0.5$); the splay and bend elastic distortions are shown in blue ($S_{\mathrm{SB}} > 0.005$) and in yellow ($S_{\mathrm{SB}} < -0.005$), respectively. e-h) The top views of director fields corresponding to a-d). f) Experimental observations of defect motions upon application of magnetic field with initial tetrahedron shell focusing on a upper right $+\frac{1}{2}$ defect.

finally merging to +1 defect (Fig 4.4h). The experimental observation of defect rotations as shown in Fig 4.4i agrees with our numerical calculations.

4.3.2 Inhomogeneous Nematic Shells

In most cases, due to the buoyancy effect and nematic elasticity, nematic LC shells are inhomogeneous with the defects located in the thinner part of the shells. Fig 4.5a and b provide schematic representations of an inhomogeneous shell from the side view and top view. The C_{2v} axis still remains as shown in Fig 4.5a, however the two C_2 axes no longer exist due to the inhomogeneity. Here we denote the C_{2v} as z axis, the directions connecting blue and red pairs as x and y axes, respectively.

We first examine the effect of the external field when it is applied along z axis (C_{2v}

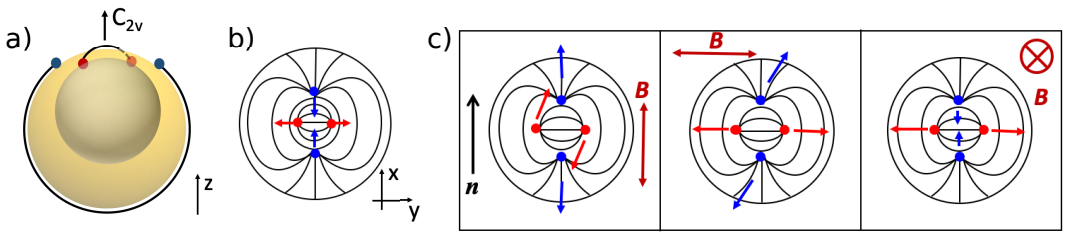

Figure 4.5: a) Schematic representation of an inhomogeneous tetravalent shell with two pairs of defects (in blue and red circles) localized in the thinner part of shells. Each pair is connected by a director streamline in black. b) Sketch of director fields of the inhomogeneous tetravalent shells with the direction of defect pair in blue denoted as x axis. The defect orientations are denoted by arrows. c) Schematic representations of defect motions when the external field is applied along x, y, and z axes.

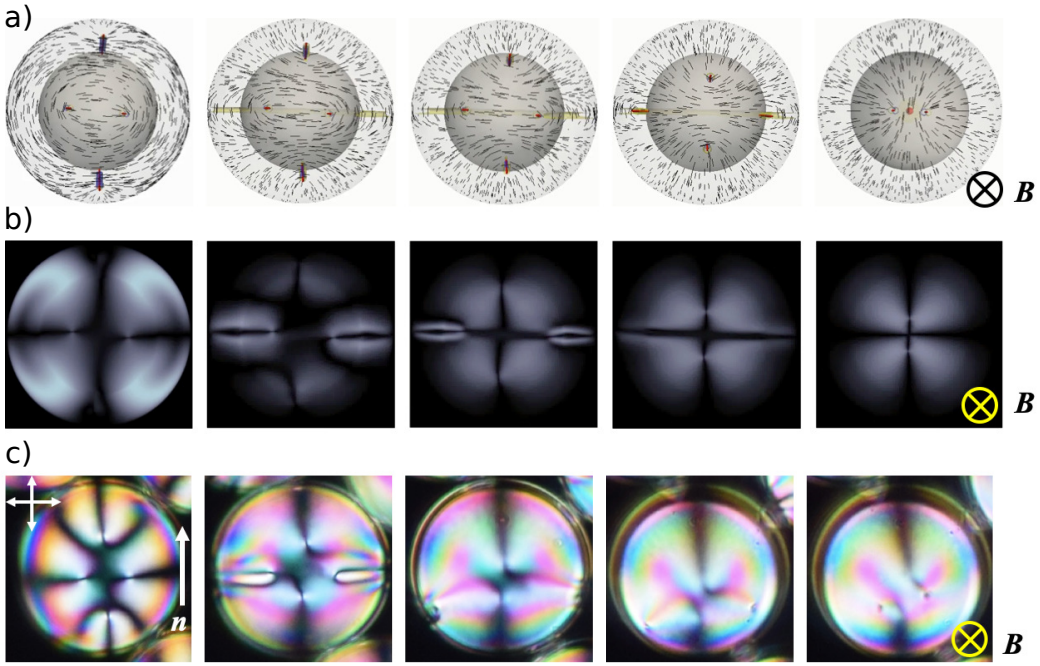

Figure 4.6: Reorientation of an inhomogeneous nematic shell under uniform magnetic field along z axis. a) The director fields on the outer surface along z axis during the evolution. The defects are shown in red (isosurface for $S = 0.5$); the splay and bend elastic distortions are shown in blue ($S_{\mathrm{SB}} > 0.005$) and in yellow ($S_{\mathrm{SB}} < -0.005$), respectively. b) The corresponding simulated polarization micrographs. c) Experimental observations of defect motions upon application of magnetic field along z axis.

axis), B_s is again parallel to the defect orientations of the four defects. The transformation, as shown in Fig 4.6, is very similar to that in homogeneous shells, except that the two disclination walls are not equal in length. In addition, due to the thickness inhomogeneity,

the final equilibrium state is a trivalent shell (Fig 3.1 e) as introduced in previous chapter. A further increase of the external field will probably provide the system enough energy to overcome the repulsion between defects in the thinner part of the shell and form a bipoalr configuration. Fig 4.6b shows the simulated polarization micrographs, where the disclination wall is clearly visible and consistent with experimental observations as shown in Fig 4.6c.

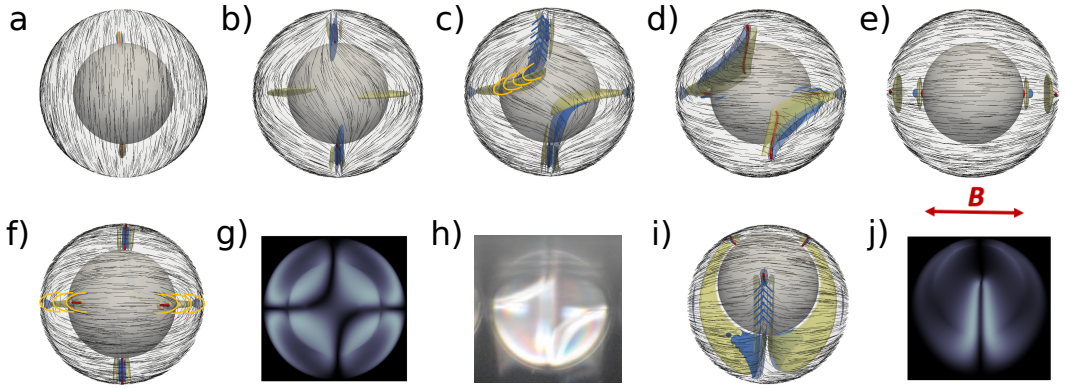

Figure 4.7: Reorientation of an inhomogeneous nematic shell under uniform magnetic field along y axis. a-e) The director fields on the outer surface along $-z$ axis during the evolution. The defects are shown in red (isosurface for $S = 0.5$); the splay and bend elastic distortions are shown in blue ($S_{\mathrm{SB}} > 0.005$) and in yellow ($S_{\mathrm{SB}} < -0.005$), respectively. f) The director field on the outer surface along $+z$ axis of configuration in c). The bend wall is highlighted in yellow. g-h) The simulation and experimental observations of polarization micrograph of the configuration in c). i) The director field on the outer surface along x axis of configuration in c). The splay wall is highlighted in blue. j) The simulation polarization micrograph of i.

When a magnetic field B is parallel to y axis, the defect orientation of red pair is parallel to B_s while that of blue is perpendicular to B_s (Fig 4.5b). According to our previous discussion about single $+\frac{1}{2}$ defect on the plane (Fig 4.2), we expect a bend wall and a splay wall emerging next to defects in red and blue, respectively. The simulated evolution of defect reorientations is shown in Fig 4.7a-e. Upon application of magnetic field, the bend wall and splay wall emerge and propagate from different defect pairs as predicted (Fig 4.7b). At certain point of time, the bend wall and splay wall join with each other and form a hybrid disclination wall (Fig 4.7c), with the bend wall mostly parallel to B_s and splay wall mostly perpendicular to B_s. It is consistent with their nature as discussed in Fig 1.6. Fig 4.7f and i provide a closer look at the director fields near the bend and splay wall from different angles.

The curved hybrid wall can also be visualized in simulated polarization micrograph (Fig 4.7g), in agreement with the experimental result (Fig 4.7h). To our knowledge, such hybrid disclination wall has not been reported yet, since it stems from curved surfaces and complex defect configurations as in this case. After the formation of hybrid disclination wall, again defects move along the wall (Fig 4.7d) and merge with the other defect (Fig 4.7e).

It is more complicated when the B is along x axis. The rule generalized from single defect predicts a splay wall between red pair, but fails in this scenario, probably due to the crowdedness of defects in the thinner part of shell. Instead, the bend wall arising from the blue pair winds back and attaches itself with the red pair, as shown in Fig 4.8a. The bend wall is more clear in the simulated polarization micrographs (Fig 4.8b). Fig 4.8i and h track the defect locations in terms of θ and ϕ of each defect pair during the evolution, where θ and ϕ are defined in the inset graphs in Fig 4.8e and f. According to their definition, θ is proportional to the distance between the defect pair and the variance of ϕ records the defect pair rotation. It shows that the blue pair moves along the B_s direction to the pole directly. While the red pair first approaches towards each other, and then moves apart when the curved bend wall forms. The red pair keeps rotating until parallel to the blue pair until the final coalescence. The experimental observations shown in Fig 4.8c-f provide a fairly good agreement of the defect motions with our simulation calculations, considering the shell size difference.

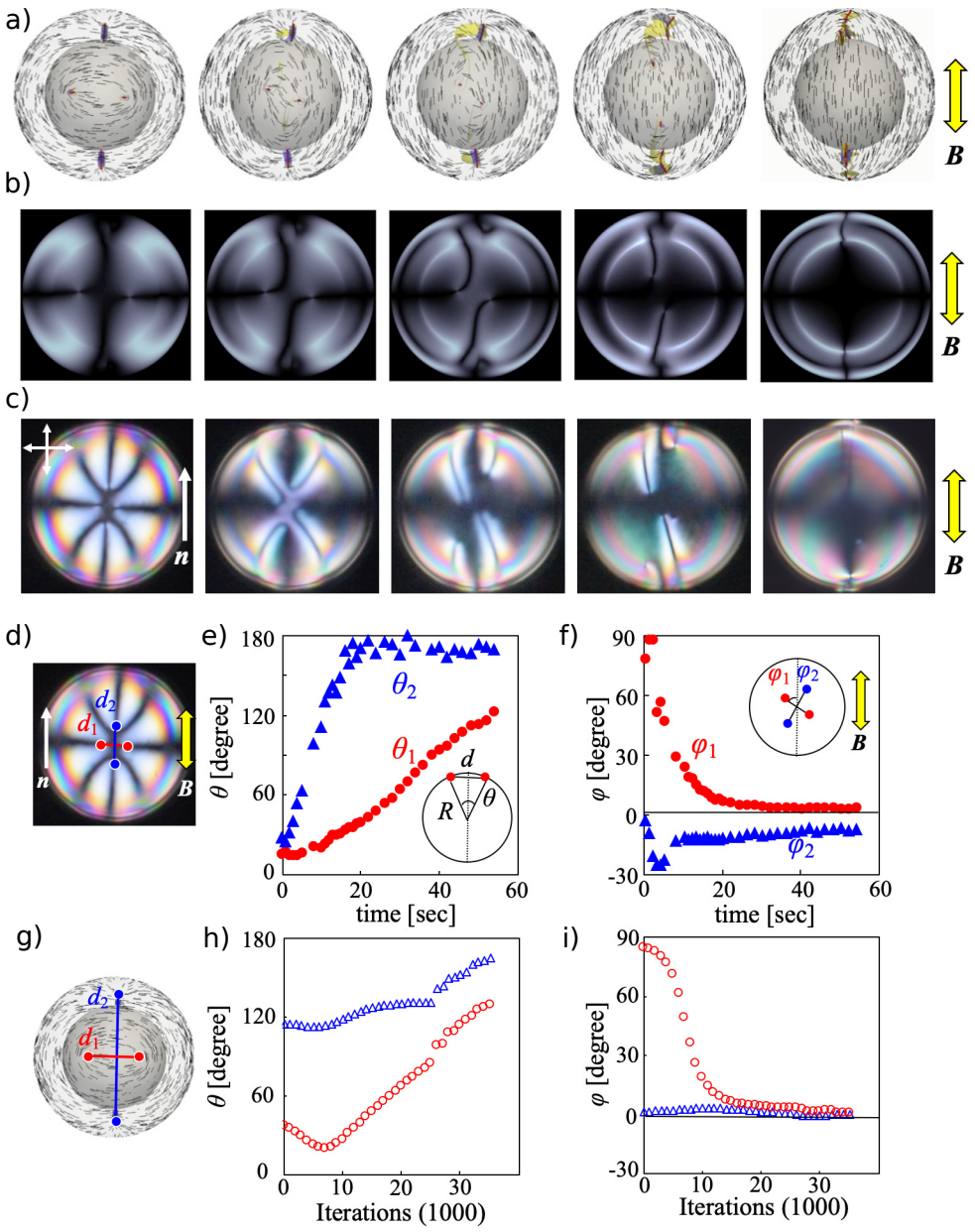

Figure 4.8: Reorientation of an inhomogeneous nematic shell under uniform magnetic field along x axis. a) The director fields on the outer surface along z axis during the evolution. The defects are shown in red (isosurface for $S = 0.5$); the splay and bend elastic distortions are shown in blue ($S_{\mathrm{SB}} > 0.005$) and in yellow ($S_{\mathrm{SB}} < -0.005$), respectively. b) The corresponding simulated polarization micrographs. c) Experimental observations of defect motions upon application of magnetic field along x axis. d) A sketch of red and blue pair defects on top of experimental image of the inhomogeneous tetravalent nematic shell. e-f) The evolution of *theta* and *phi*, as defined in the inset graphs, during the transformation in experiments. g) A sketch of red and blue pair defects on top of simulated director field of the inhomogeneous tetravalent nematic shell. h-i) The evolution of *theta* and *phi* during the transformation in simulation.

CHAPTER 5
MODELING OF DEGENERATE CONIC ANCHORING AND COLLOIDAL ELASTIC DIPOLE-HEXADECAPOLE TRANSFORMATIONS

5.1 Introduction

Nematic colloids - colloidal particles immersed in a liquid crystal (LC) host, have been studied extensively over the past decade [52, 31, 43, 71, 69, 41, 24, 61, 46]. Seminal experiments by Poulin et al. [52] reported striking observations pertaining to strong and long-range structural forces between nematic colloids, which arise from the anisotropy of the media [54, 57, 32]. A more quantitative characterization of these elasticity-mediated forces was conducted years later using a dual-beam laser trap [81, 70]. With a deeper understanding of the structural forces that arise between colloids in nematic materials, it has been possible to study the formation and characterization of a variety of self-assembled structures in one-dimension (linear chains) [52, 31], two dimensions [43, 41] and three dimensions [46, 38], paving the way for potential applications in photonics [40]. Such assemblies have also had an impact in other scientific domains, including optical manipulation of nematic colloids [39, 74], knot theory [7], and memory effects [42].

For years, only three possible defect configurations were reported for spherical nematic colloids: one with two surface point defects (boojums) at the poles, for colloids with tangential (degenerate planar) anchoring, Saturn-ring configurations with a disclination ring in the bulk at the equator, and dipolar configurations with a bulk point defect (hyperbolic hedgehog) for colloids having homeotropic anchoring [32, 15, 30, 72, 41]. Quadrupolar (boojums and Saturn ring configurations) and dipolar (a hedgehog configuration) symmetries severely limit the possibilities of formation of colloidal bonds and self-assembly. Recently, an elastic hexadecapole was created by relying on an insightful analogy to electrostatic charge distribu-

tion [62]. It was suggested that the new symmetry stems from a degenerate conic anchoring condition imposed at the colloid surface (where conic alignment has easy axes along a conic surface at a specific polar angle (θ_e) [63, 55, 10]).

To better understand this new defect structure, and to help design novel colloidal lattices, new models must be developed that are capable of describing this type of anchoring and its consequences for defect formation. With that goal in mind, a continuum model is introduced here for the order parameter tensor $\mathbf{Q}$. By incorporating that model into a Landau-de Gennes theory, we are able to conduct a systematic study of nematic colloids with degenerate conic anchoring and the corresponding defect structures as a function of θ_e. In the first section, we investigate the elastic hexadecapole, and characterize its region of stability in terms of θ_e. The angular and radial dependence of the elasticity-mediated interactions between colloids are unique for different θ_e. Moreover, a new elastic dipole species is predicted for nematic colloids with degenerate conic anchoring and validated in experiments. Our calculations provide useful insights concerning the meta-stability of this elastic dipole with increasing θ_e, and its transition into an elastic hexadecapole, as observed in experiments.

5.2 Model and methods

5.2.1 Simulation details

In this work, we propose a different model to represent degenerate conic anchoring, in which the surface free energy is written as

$$f_{\text{surf}}^{c} = \int_{\text{surf}} W_c \left(P'_{ik} \tilde{Q}_{kl} P'_{lj} - S_{\text{eq}} cos^2\theta_e P'_{ij} \right)^2 d\Sigma. \tag{5.1}$$

Here W_c is the anchoring strength for degenerate conic anchoring, $P'_{ij} = \nu_i \nu_j$ is the new projection tensor, and θ_e is the angle between n_e and ν (Fig 1a). Assuming that there is no

spatial variation of the scalar order parameter ($S \equiv S_{\text{eq}}$):

$$\begin{aligned}\left(P'_{ik}\tilde{Q}_{kl}P'_{lj} - S_{\text{eq}}cos^2\theta_e P'_{ij}\right)^2 &= (\nu_i\nu_k S_{\text{eq}} n_k n_l \nu_l \nu_j - S_{\text{eq}}\cos^2\theta_e \nu_i\nu_j)^2 \\ &= (\nu_i\nu_j S_{\text{eq}}\cos^2\theta_s - \nu_i\nu_j S_{\text{eq}}\cos^2\theta_e)^2 \\ &= S_{\text{eq}}^2(\cos^2\theta_s - \cos^2\theta_e)^2 \nu_i\nu_j\nu_i\nu_j \\ &= S_{\text{eq}}^2(\cos^2\theta_s - \cos^2\theta_e)^2.\end{aligned} \tag{5.2}$$

Therefore,

$$f_{\text{surf}}^{c,\theta_s} = \int_{\text{surf}} W_c S_{\text{eq}}^2(\cos^2\theta_s - \cos^2\theta_e)^2\, d\Sigma. \tag{5.3}$$

Here θ_s is the angle between the surface director and surface normal, defined as $\cos\theta_s = n_i\nu_i$.

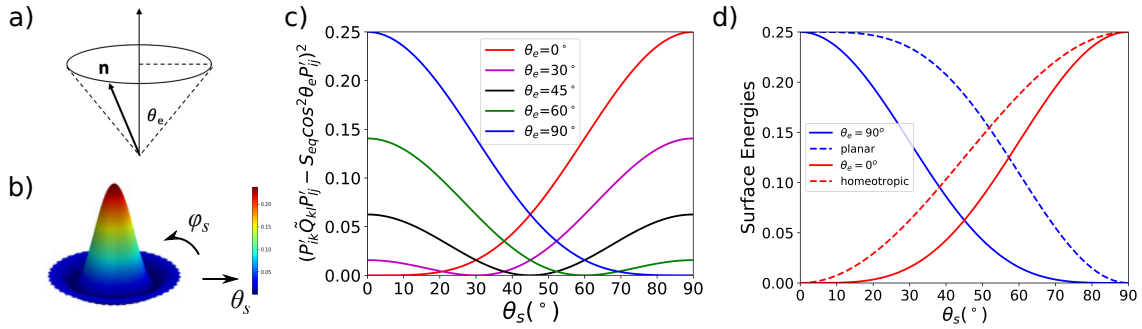

Figure 5.1: a) Schematic representation of degenerate conic anchoring with preferred tilt conic angle θ_e. b) Schematic representation of free energy of degenerate conic anchoring with degeneracy in the azimuthal angle ($\theta_e = 60°$). c) Values of $(P'_{ik}\tilde{Q}_{kl}P'_{lj} - S_{\text{eq}}cos^2\theta_e P'_{ij})^2$ as a function of θ_s for $\theta_e = 0°, 30°, 45°, 60°$, and $90°$ with $S_{\text{eq}} = 0.5$. d) Comparison between the surface free energy term of $\frac{1}{2}\left(Q_{ij} - Q^0_{ij}\right)^2$ in Equation 1.25, $\left(\tilde{Q}_{ij} - \tilde{Q}^{\perp}_{ij}\right)^2$ in Equation 1.26 and $(P'_{ik}\tilde{Q}_{kl}P'_{lj} - S_{\text{eq}}cos^2\theta_e P'_{ij})^2$ in Equation 5.1 with $\theta_e = 0°, 90°$ as a function of surface tilt angle ($S_{\text{eq}} = 0.5$).

The transformation reveals the fact that the surface free energies f_{surf}^c is minimized when $\theta_s = \theta_e$, consistent with its degenerate conic anchoring type (Fig 5.1a). Here we note that other, simpler θ-based expressions for degenerate conic anchoring have been employed in the literature [63, 55]. Such expressions do not allow one to describe the defects engendered by conic anchoring. The **Q**-tensor expression proposed here, however, is superior in that it

can capture the surface ordering, thereby permitting a description of the defects that arise in our systems, which is essential for our work and, more generally, for detailed studies of nematic colloids. Figure 5.1c shows the evolution of $(P'_{ik}\tilde{Q}_{kl}P'_{lj} - S_{\mathrm{eq}}cos^2\theta_e P'_{ij})^2$ in f^c_{surf} as a function of surface director tilt angle θ_s for a range of preferred tilt angles. Again, these results demonstrate that, guided by the **Q** tensor-based Equation 5.1 proposed here, the surface directors favor orientation along a conic plane with an angle θ_e to the surface normal.

When compared to Equations 1.25 and 1.26, Equation 5.1 provides a universal expression for surface free energy, since, in some sense, homeotropic and degenerate planar surface anchorings represent individual cases of degenerate conic anchoring for a 'collapsed cone' ($\theta_e = 0^\circ$) or a 'flat cone' ($\theta_e = 90^\circ$):

$$f^{c,\,\theta_s}_{\mathrm{surf}} = \begin{cases} \int_{\mathrm{surf}} W_c S^2_{\mathrm{eq}} \sin^4\theta_s \, d\Sigma. & \theta_e = 0^\circ, \\ \int_{\mathrm{surf}} W_c S^2_{\mathrm{eq}} \cos^4\theta_s \, d\Sigma. & \theta_e = 90^\circ, \end{cases}$$

Fig 5.1d illustrates the distinction between these expressions; degenerate conic anchoring (Equation 5.1) imposes a lesser energy penalty for deviations of the directors from their preferred direction than Equations 1.25 and 1.26.

The following numerical parameters were used: $A = 1.17 \times 10^5\,\mathrm{J/m^3}$, $U = 3.5$, $L = 6 \times 10^{-12}$ N, $W_c = 10^{-3}\,\mathrm{J/m^2}$, unless specified otherwise. The channels in this work have periodic boundaries along the x and y axes, and rigid homeotropic anchoring along the z-axis.

5.2.2 Experiment details

Glycerol (Sigma-Aldrich) droplets were suspended in a nematic LC 5CB (4-cyano-4'- pentylbiphenyl from Frinton Laboratories, Inc.) with a small amount (< 0.1 vol.%) of a molecular surfactant (sodium dodecyl sulfate) mixed with glycerol. The mixture of glycerol (about 10

vol.%) and 5CB was vigorously stirred to obtain glycerol spherical droplets ($R \approx$1-10 μm) dispersed evenly in the LC host. Dispersions were filled into approximately 30 μm-thick cells made of two glass plates separated by glass spacers and sealed with a UV-curable glue. A polyimide PI2555 (HD Microsystems) was spin-coated on the glass plates, baked at 270°C and unidirectionally rubbed with a velvet cloth to create a homogeneous planar alignment of the LC. Experimental samples were stable over at least several weeks and the director structures around the droplets were studied using bright field and polarized light optical observations with a 100×(NA = 1.42) oil objective mounted on an inverted Olympus IX81 microscope. Image acquisition and analysis were performed using a CCD camera (Flea, PointGrey) and ImageJ software, respectively.

5.3 Results and Discussion

5.3.1 Elastic Quadruple and Hexadecapole

Using the **Q**-tensor-based surface energy term (Equation 5.1), one can perform simulations of an individual particle ($R = 250\,\text{nm}$) with degenerate conic anchoring confined in a nematic channel ($h = 1.5\,\mu\text{m}$). The inclusion of colloids with curvature inevitably leads to orientational frustration, generating point defects or disclination lines as a result. In agreement with previous experimental work [62], the nematic colloidal particle with degenerate conic anchoring ($\theta_e = 45°$) exhibits two boojums at the poles and a defect ring at the equator, resembling a combination of defect configurations of colloids with $\theta_e = 0°$ and 90° (Fig 5.2a). Moreover, as shown in Fig 5.2c, the n_x color maps for nematic colloids with $\theta_e = 0°$and 90° both exhibit quadruple symmetry, while that for $\theta_e = 45°$ shows an hexadecapolar symmetry, similar to a superposition of two quadruples of opposite sign.

In terms of polarized light micrographs, a uniform LC channel appears all dark when the far-field director $\mathbf{n}_0$ is parallel to the polarizer or analyzer, while the perturbation induced by the inclusion of colloids may lead to brightness. For instance, the lobes in the micrographs

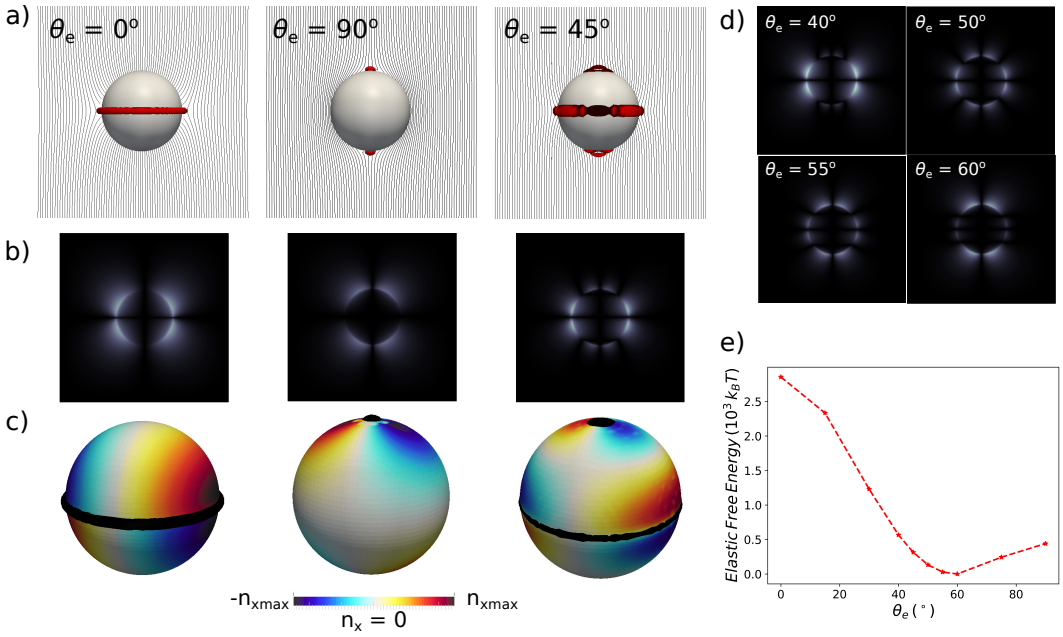

Figure 5.2: a) Director fields for nematic colloids ($R = 250$nm) with $\theta_e = 0°, 90°$, and $45°$, respectively. Defects are shown in red (isosurface for S = 0.6). b) Simulated polarized light micrographs for nematic colloids with $\theta_e = 0°, 90°$, and $45°$. The brightness of the images for $\theta_e = 0°$ and $90°$ is reduced by half for the purpose of comparisons. The far field director is parallel to the polarizer or analyzer. c) Color map of the directors' x-component (n_x) on the colloidal surface. d) Simulated polarized light micrographs for nematic colloids with $\theta_e = 40°, 50°, 55°$, and $60°$. e) Elastic free energy for nematic colloids with increasing θ_e.

(Fig 5.2b) for colloids with $\theta_e = 0°$ (homeotropic) and $\theta_e = 90°$ (degenerate planar) correspond to elastic distortions surrounding the disclinations. Interestingly, the polarization graph of a colloid with $\theta_e = 45°$ displays eight separated lobes near the colloidal surface; these observations are consistent with the key optical features of the elastic hexadecapole reported in the recent literature [62]. More importantly, Fig. 5.2d shows that the relative brightness of the eight lobes varies with θ_e, providing a potential methodology to measure θ_e in experiments (SI). Note that, in Fig 5.2b, the brightness for colloids with $\theta_e = 0°$ and $90°$ has been reduced by half for the purpose of comparisons, implying greater elastic deformations compared to those in elastic hexadecapoles. This is further illustrated by the elastic free energy analysis of nematic colloids with increasing θ_e, which shows a minimum of elastic energy near $\theta_e = 60°$ (Fig 5.2e).

5.3.2 Interactions between elastic multiples

At the next level of complexity, we consider the elasticity-mediated interactions that arise between nematic colloids with different θ_e, which are central to understanding colloidal self-assembly. The two particles are confined in a uniform LC channel. As illustrated in Fig 5.3b, the inter-particle separation is denoted by d and the angle between the uniform far-field nematic director and particle-particle vector is given by α.

As a means to validate our calculations, we first consider the elastic interactions between colloids with degenerate planar anchoring ($\theta_e = 90^\circ$). Fig 5.3a shows the free energy for a two-particle system, at different colloidal separations d/R and different orientations α. As colloidal separation d/R increases from 2.4 to 3.4, the α corresponding to the minimum energy, defined as α^*, gradually shifts from 30° to 45°, as shown in the inset of Fig 5.3a. The vector field of forces in Fig 5.3b shows more clearly that the colloids attract each other for $\alpha < 70^\circ$ and repel each other for $\alpha > 70^\circ$ with $d/R = 2.6$. As particles move apart from each other, the forces become weaker, and the attraction direction migrates to α near 45° for $d/R = 3.2$. These findings are in agreement with past literature reports [70, 37].

In order to understand how elasticity-mediated interactions change as the preferred tilt angle θ_e is varied, we fix the colloidal separation ($d/R = 2.4$) and plot the angular dependence for interactions as a function of α, for different θ_e. Results are shown in Fig 5.3c. Similar to the colloids with degenerate planar anchoring, colloids with $\theta_e = 0^\circ$ have one energy well at $\alpha^* = 65^\circ$, consistent with past reports [41]. Instead of a simple shift of the energy well from $\alpha^* = 65^\circ$ ($\theta_e = 0^\circ$) to $\alpha^* = 30^\circ$ ($\theta_e = 90^\circ$), a double-well state appears between $\theta_e = 40^\circ$ and 60° (Fig 5.3c). It is within the same range of θ_e, where the eight-lobe pattern in polarized optical images (Fig 2d) becomes pronounced. At $\theta_e \sim 55^\circ$, the depths of the two energy wells are approximately identical; as shown in the inset of Fig 5.3c, the α^* corresponding to the deepest well switches from 70° to 20° at $\theta_e \sim 55^\circ$.

The dependence of this double-well energy profile on colloidal separation d is examined in closer detail for colloids with $\theta_e = 45^\circ$. Results are shown in Fig 5.3d-e. In contrast to

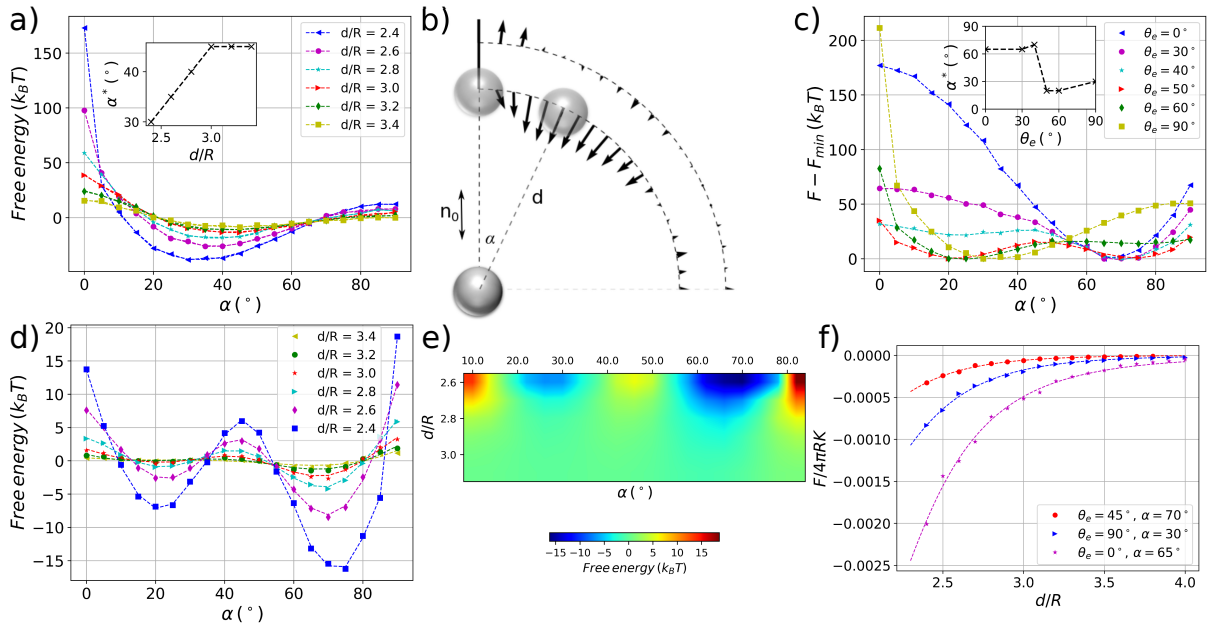

Figure 5.3: a) Free energy as a function of α for different inter-particle separations d/R for $\theta_e = 90°$ for two particles ($R = 200\,\text{nm}$) confined in a uniform LC channel ($h = 3.6\,\mu\text{m}$). The inset plot shows the dependence of α^* on the colloidal separation d. b) Vector field of forces between two colloidal particles for $d/R = 2.6$ and 3.2. The far-field director is denoted by $\mathbf{n}_0$. c) Evolution of free energy as a function of α with different θ_e ($d/R = 2.4$). The inset plot shows the dependence of α^* on colloidal separation d. d) and e) Evolution of free energy as a function of α for different d/R with $\theta_e = 45°$. f) Dependence of attraction on d/R for particles with $\theta_e = 45°, 90°$, and $\theta_e = 0°$, along $\alpha = 70°, 30°$, and $65°$. The dashed line is a least-squares fit of colloidal pair interactions. The coefficients are ($b_2 = -0.0088, b_4 = -0.0144, b_6 = -0.0004$), ($b_2 = -0.0496, b_4 = -0.0089, b_6 = -0.0005$), ($b_2 = 0.1001, b_4 = -0.0105, b_6 = 0.0009$) for colloids with $\theta_e = 45°, 90°$, and $\theta_e = 0°$, respectively.

colloids with simple degenerate planar anchoring, the two energy wells corresponding to the elastic hexadecapoles are basically localized near $\alpha = 20-25°$ and $\alpha = 70-75°$ for increasing colloidal separations. This indicates that the forces between elastic hexadecapoles, be they attractive or repulsive, are basically along the radial direction. Taken together, our results therefore show that both the nature of colloidal interactions (attractive/repulsive) and their dependence on α and d are governed by the angle θ_e at the colloidal surface. This finding suggests that new avenues that rely on manipulation of this angle may be used to control the formation of new and diverse colloidal assemblies.

A similar analysis of the elastic multipole moments as that performed in recent experi-

ments [62] is conducted here by a least-squares fit to the theoretical colloidal pair-interactions (Equation 5.4), derived from an electrostatic analogy of the far-field director distortions.

$$U_{int} = 4\pi K \sum_{l,l'=2,4,6} a_l a'_{l'} (-1)^{l'} \frac{(l+l')!}{R^{l+l'+1}} P_{l+l'}(\cos\theta) \tag{5.4}$$

where $a_l = b_l r_0^{l+1}$ represents the elastic multipole moment of the lth order (2^l-pole).

The ratios of elastic quadruple moment (b_2) to hexadecapole moment (b_4), obtained from fitting (Fig 5.3f), are $0.61, 5.57, -9.53$ for nematic colloids with $\theta_e = 45°, 90°,$ and $0°$, respectively. These results serve to emphasize the fact that quadruple moments (with opposite signs) are dominant at $\theta_e = 0°$and $90°$, and they cancel each other at around $\theta_e = 45°$, thereby letting the hexadecapole symmetry stand out.

5.3.3 Elastic Dipole

By initializing a different, specific condition (Equation 1.49), we also predict another candidate structure for nematic colloids having degenerate conic anchoring (CA): we refer to this structure as an 'elastic CA dipole' to distinguish it from the more commonly studied elastic dipole formed by colloids with perpendicular surface boundary conditions.

As shown in Fig 5.4a, a nematic colloid with homeotropic anchoring ($\theta_e = 0°$), which adopts a homeotropic anchoring (HA) dipole configuration, possesses a bulk hedgehog defect at the upper pole. As the anchoring becomes conic ($\theta_e > 0°$), a boojum emerges at the lower pole (*e.g.* Fig 5.4b). Since all the structures of the director field around colloidal particles considered here have axial symmetry with respect to the far-field director, for simplicity, it is possible to analyze topological charge conservation in terms of 2D defect topological charges within the plane containing $\mathbf{n}_0$. In terms of such 2D charges, it is known that colloids with homeotropic anchoring carry a charge of $q = +1$; since the charge of the hedgehog defect in a dipolar configuration is $q = -1$, the total equals zero [71]. Nematic colloids with degenerate conic anchoring also carry a 2D effective charge of $q = +1$ (SI). Fig 5.4b shows the defect

configuration for a nematic colloid with $\theta_e = 45^\circ$, where the defect strength (-1) is unevenly distributed amongst upper $(-3/4)$ and lower surface defects $(-1/4)$ while complying with the conservation of charges, as before. The formation of a boojum in nematic colloids with degenerate conic anchoring can also be visualized in simulated polarized light micrographs (Fig 5.4c-d). The position of the two lobes on top of the colloids exhibits another significant distinguishing feature: for HA dipoles (Fig 5.4c), the lobes spread out evenly along the vertical axis, while those in CA dipoles (Fig 5.4d) are closer to the upper defect of $-3/4$.

Experiments on colloidal particles were used to verify our numerical predictions (Fig. 5.4b,d). Most of the observed droplets had homeotropic anchoring with a typical dipolar configuration of the director (Fig 5.4a,c,e). However, a small number of particles showed a hexadecapolar texture (Fig. 5.2), characteristic of conic anchoring, or a texture with a hedgehog point defect at one pole of the droplet and a boojum point defect at the other pole (Fig. 5.4b,d,f,g). At first sight, the latter director field around the droplet resembles the dipolar configuration around particles with homeotropic anchoring. However, upon more careful observation, one can see that the elastic CA dipole observed in this experiment has several subtle differences. First, there are two weakly bright lobes surrounding the dark point of the boojum defect at the pole opposite to the one with the hedgehog (compare Fig. 5.4e and f,g; pointed by Arrow 1). The dark point corresponding to the boojum defect is poorly visible in the textures with parallel polarizers, as the scattering from it is weak and blends together with strong scattering from the droplet contour. Secondly, there is a sequence of dark and bright brushes at the pole with a hedgehog in the typical HA dipole (pointed out by Arrow 2). Lastly, two bright areas within the polarized texture of the droplet and two corresponding dark areas in the texture between parallel polarizers (pointed respectively by arrows 3 and 4 in Fig. 5.4e-g) extend from the top to the bottom pole in the typical HA dipole. However, in the elastic CA dipole in our experiments, they are located mostly in the hemisphere with the hedgehog defect. The good agreement between polarized light textures of the elastic CA dipole observed in the experiments and predicted in our calculations serves

to confirm the conic anchoring that we have at the surface of the droplets and, importantly, supports the proposed model of surface free energy for degenerate conic anchoring.

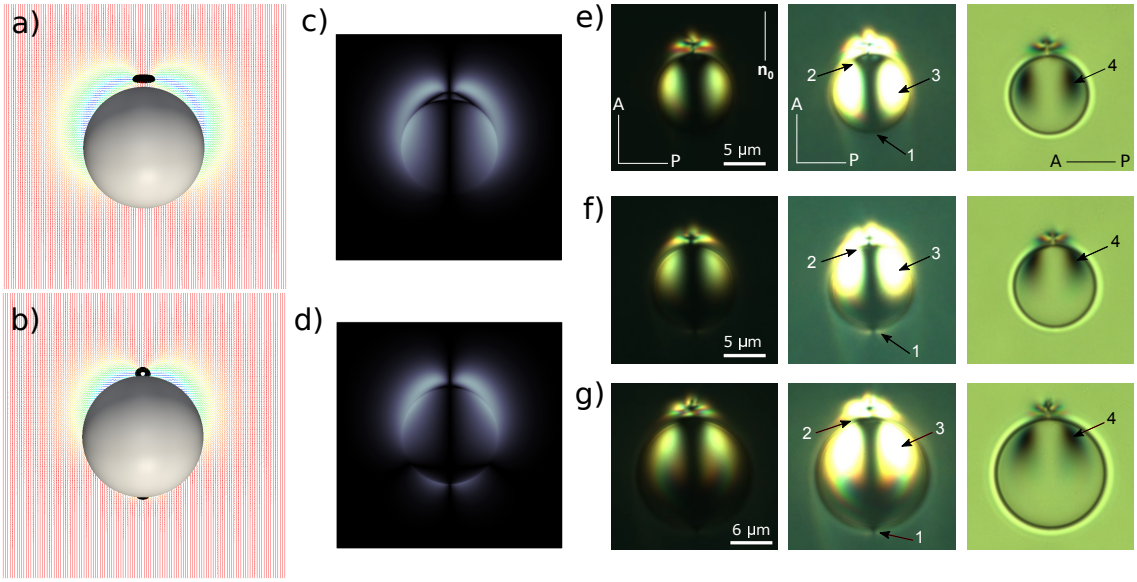

Figure 5.4: a-b) Director fields for dipole colloids ($R = 750\,\text{nm}$) with $\theta_e = 0°$ (a) and 45° (b), colored by its projection onto the z-axis. The defects are shown in black (isosurface for S = 0.6). c-d) Corresponding polarized light micrographs of dipole colloids with $\theta_e = 0°$ (c) and 45° (d). e-g) Optical microscopy textures of a dipole with homeotropic (e) and conic (f, g) anchoring, which are consistent with the predicted textures shown in (a, c) and (b, d), respectively; $\mathbf{n}_0$ shows a far-field director set by rubbing. Left and middle textures in (e-g) were taken between crossed polarizers A and P; textures in the middle are slightly overexposed to enhance visibility of boojums at the bottom pole. Textures in the right column were taken between parallel polarizers.

5.3.4 The transition from Elastic Dipole to Hexadecapole

It is difficult in experiments to observe the elastic CA dipole for large θ_e. Upon disturbing the system, it evolves spontaneously into a more stable elastic hexadecapole (Fig. 5.5j). Our calculations also predict a vanishing energy barrier between elastic CA dipoles and hexadecapoles as θ_e increases and becomes larger than 45°. This is to be expected, because as θ_e increases to 90°, the nematic colloid has no choice but to adopt a quadrupolar symmetry. To understand this transition, we perturb an equilibrium CA dipole configuration with $\theta_e =$ 45° by setting θ_e to 60°, and monitor the ensuing relaxation process (Fig 5.5a-h). In the

early stages, the CA dipolar colloid with $\theta_e = 60°$ distributes the 2D charge $q = -1/3$ to the lower pole defect and $q = -2/3$ to the upper pole defect (Fig 5.5a). Subsequently, a surface defect ring of $q = -1/3$ splits out from the upper pole defect and gradually migrates downwards. As the defect ring arrives at the equator, it forms an elastic hexadecapole (Fig 5.5d).

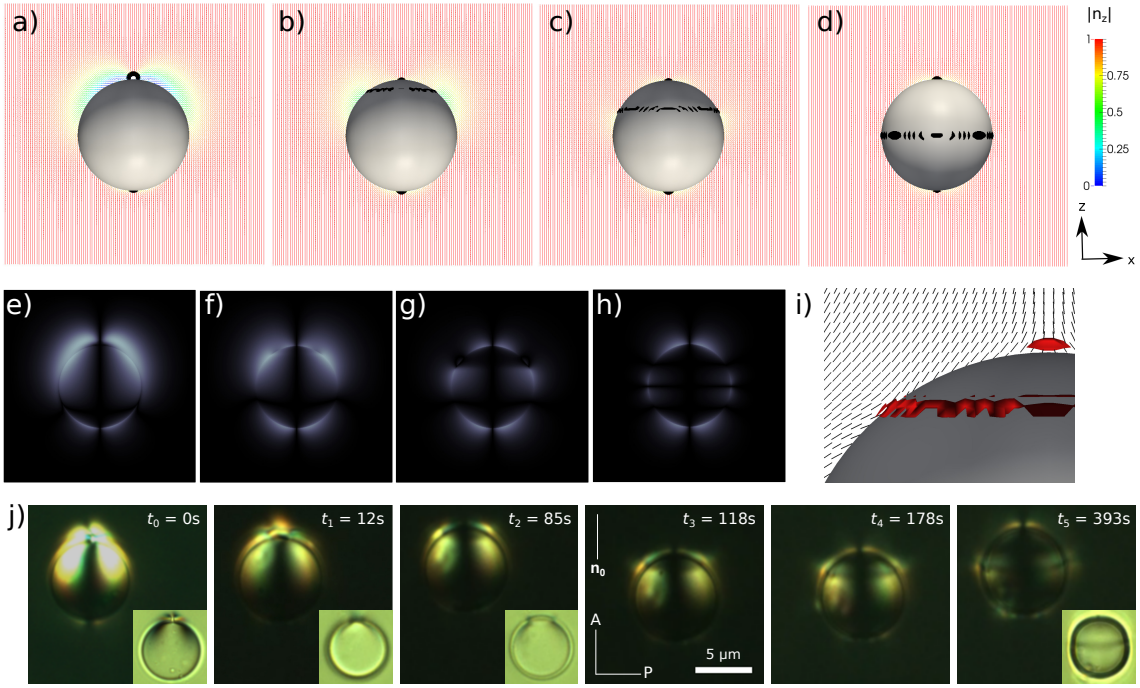

Figure 5.5: a-d) A temporal sequence of configurations during relaxation after applying $\theta_e = 60°$ to an equilibrium elastic dipole of $\theta_e = 45°$. The director field is colored by its projection onto the z-axis, and the defects are shown in black (isosurface for S = 0.6). e-h) Corresponding simulated polarized light textures. i) Director field near the defect ring in b). The director field is shown in black and the defects are shown in red (isosurface for S = 0.6). j) Experimental sequence of microscope textures showing the transition from a dipolar to a hexadecapolar structure taken between crossed polarizers. The first texture is slightly overexposed compared to the others in order to enhance the visibility of a boojum defect at the bottom pole. Insets show corresponding textures taken between parallel polarizers. The size of the bottom side of the inset image is 9.5 μm.

Fig 5.5i provides a closer look at the director field near the defect ring. Since the director profiles along the x-z cross section are all in plane, the easy cone that is observed in 3D collapses onto two easy axes (clockwise and counter-clockwise) for $\theta_e = 60°$. In the CA dipolar configuration, the directors lie along the clockwise easy axis on the right and along

the counter-clockwise easy axis on the left side of the colloidal surface, varying continuously from one pole to the other. Fig 5.5i shows that the directors on top of the defect ring (left side) have flipped from their original counter-clockwise to their clockwise easy axis. Therefore, the transition proceeds by gradually flipping the directors between two easy axes along the z-axis. As a consequence, we observe that the defect ring, which results from the orientational discontinuity at the flipping boundary, moves towards the equator.

The transition from the CA dipolar to the hexadecapolar structure predicted on the basis of our model is also observed in our experiments (Fig. 5.5j). Right after filling the dispersion into the observation cells, the CA dipolar structure described above (Fig. 5.5a,e) prevails around droplets with conic anchoring. The boojums resulting from conic anchoring scatter less light when compared to typical boojums in particles having tangential anchoring [70]; note that their weak scattering blends with strong scattering from the droplet's contour, which explains why boojums are only slightly visible in the bright field textures of our droplets. However, bright lobes around the boojums, caused by having the director field around them be tilted with respect to $\mathbf{n}_0$, are clearly visible in textures taken between crossed polarizers. After a while, that CA dipolar structure (see a texture at t_0) spontaneously changes to the hexadecapolar configuration (see a texture at t_5). The transition starts at the top pole from the hedgehog, breaking up into a boojum, similar to the one on the bottom pole, and a surface disclination ring (see a texture at t_2 and the calculated director field in Fig. 5.5i). A surface disclination ring, which can clearly be appreciated in the microscopic textures as a darker, blurred line, gradually extends and moves towards the equator of the droplet ($t_1 - t_5$). The transition is quite slow, and is completed when the surface disclination reaches the equator of the droplet (t_5), within 5 to 10 minutes from the start of the process. The predicted textures for the structural transition are in good agreement with experiment, serving to underscore the validity and the significance of the proposed model for the surface free energy under degenerate conic anchoring.

CHAPTER 6

CONCLUSIONS

The focus of this thesis is to use a Landau–de Gennes continuum model to simulate nematic systems, in order to systematically study the effect of chirality in a confined geometry, external field on the defect configuration, and degenerate conic anchoring condition.

The second chapter mainly investigate the structural transition in cholesteric liquid crystal droplets. In the first section, for strong anchoring we recovered the twisted bipolar structure (TBS) and the radial spherical structure (RSS) for low ($N \leq 3$) and high ($N > 4$) chirality systems, respectively. A detailed analysis of the continuous transition from TBS to RSS that occurs within a narrow range of chirality ($3.3 \leq N \leq 4$) revealed the existence of a bent structure, in agreement with our experimental observations. A decomposition of the bent structures' free energies into splay, twist and bend deformations, was then used to show that the balance between elasticity and chirality is responsible for the gradual bend of the ChLC droplets with chirality. In the second section of this work, we examined the effect of anchoring strength on the structure of ChLC droplets and found that for weak anchoring ($W \sim 10^{-7} - 10^{-6}\,\mathrm{J/m^2}$), the system adopts a director structure similar to the equilibrium helical phase formed in the bulk. As W increases to $10^{-5}\,\mathrm{J/m^2}$, the directors near the surface deform considerably, leading to the formation of the planar bipolar structure (PBS). Further increases of the anchoring strength eventually trigger a morphological transition from the PBS to the bent structure at $N = 3.5$. Taken together, our results serve to emphasize that ChLC droplet configurations are particularly sensitive to chirality (N) and surface anchoring (W). Chirality, on the one hand, is in turn dependent on a variety of environmental conditions, including temperature and chiral dopant concentration, thereby providing a mechanism for tuning the response of a droplet. Surface anchoring, on the other hand, can be altered substantially through the interaction of adsorbates with ChLC droplets, and induce transitions that could be used for facile sensing based on optical measurements. In future work, we will present a study of ChLC droplet response to different surface active

molecules and nanoparticles based on the findings presented in this work.

The third chapter conducts a systematic study has been presented of non-chiral and chiral nematic LC shells ($R = 1\,\mu$m) with strong planar degenerate anchoring ($W = 10^{-3}\,\mathrm{J/m^2}$). In uniform non-chiral nematic shells, as shell thickness varies, a transition between a bipolar structure (BS) and a tetravalent structure (TeS) occurs near $u^* = 0.5$. For asymmetric shells ($\Delta \neq 0$), defect configurations can vary considerably. The energetically favored inner drop positions correspond to locations in the periphery of the outer drop. For uniform chiral shells ($\Delta = 0$), a phase diagram was presented that includes several novel defect configurations, namely tetravalent structure (TeS), bipolar structure (BS), bent structure (BeS) and radial spherical structure (RSS). To characterize these, a new parameter $c = h/p$ was introduced, which measures chirality in shell geometries. Values of $c = 0.125$ and $c = 0.75$ characterize the TeS-BS and BS-RSS phase boundaries, respectively. It is important to emphasize the sharpness of the BS-RSS transition in response to both chirality and shell geometry, which suggests potential uses for triggerable materials. By examining the elastic forces on the inner drop for intermediate chirality ($N = 4$) and high chirality ($N = 8$), it was shown that the degree of asymmetry of stable configurations for different thicknesses is governed by shell chirality c. Note that in this work the radius R of the drop was fixed, and both surfaces (inner and outer drops) were assumed to exhibit strong degenerate planar anchoring. Many parameters remain to be investigated, including curvature, boundary conditions and temperature. Recent numerical work, for example, has revealed intriguing defect patterns when BPs are confined in slits with thickness comparable to the unit cell size [13]. Such systems and others will be considered in a future study.

The fourth chapter examines the defect reorientation in both homogeneous and inhomogeneous tetravalent nematic shells under uniform strong magnetic fields applied in different directions. It first confirms the possibility of controlling defect number and defect valence via external fields. Furthermore, by analyzing the defect motions during the transformation, we noticed that when B_s is parallel to defect orientations ($B \parallel C_{2v}$), straight bend walls emerge

between defect pairs. While when there is some angle between B_s and defect orientations ($B \parallel C_2$), it forms S-shape bend walls, leading to the rotation of defects. With inhomogeneous tetravalent shells, we further justify our hypothesis and observed a hybrid-splay-bend wall for the first time. Our simulation results are confirmed by the experimental observations, validating the role of disclination walls in the mechanism of defect reorientation under the effect of external fields. Therefore, we may conclude that the formation of the disclination walls highly depends on the relative orientation between B_s and defect orientations and it governs the defect motions induced by the external fields. A better understanding of this mechanism may provide new methods to not only control the defect position, number and valence, but also manipulate the defect dynamics.

The last chapter has been proposed here for degenerate conic anchoring at liquid crystal interfaces. With that model, it has been possible to investigate systematically two types of nematic colloids, with $0^\circ \leq \theta_e \leq 90^\circ$. For these anchoring angles, one forms an elastic quadrupole/hexadecapole and an elastic dipole. The elastic hexadecapole was first reported in recent experiments; our calculations are consistent with such measurements[62]. Equipped with this new model, we were able to vary θ_e continuously, thereby going beyond past experimental observations. New dipolar configurations were identified, and these structures were confirmed in experiments, serving to highlight the usefulness of the proposed model. From a theoretical point of view, we introduced an explanation for our observations that relies on vanishing energy-barriers for the meta-stability of certain structures with increasing θ_e, and we followed this transition to an elastic hexadecapole as $\theta_e > 45^\circ$. By monitoring the destabilization of the elastic conic anchoring dipole, we also proposed a transition mechanism based on 'director-flipping-boundary defect rings'. That mechanism was also confirmed in our experiments. Beyond single colloid structures, we also showed that each θ_e defines a unique defect configuration, with a corresponding polarized light micrograph, and a specific angular/radial dependence for two-body colloidal interactions. Based on the relative brightness of the eight-lobe pattern in the polarized micrographs for colloids with different

θ_e, for example, one may engineer new approaches to measure the preferred tilt angle on the colloidal surface via image-recognition techniques. Moreover, the improved understanding of specific inter-particle interaction for each θ_e presented here offers the potential to define new protocols for design of self-assembled nematic colloid structures having new symmetries.

REFERENCES

[1] Janez Bezić and Slobodan Žumer. Structures of the cholesteric liquid crystal droplets with parallel surface anchoring. *Liq. Cryst.*, 11(4):593–619, 1992.

[2] Y. Bouligand and F. Livolant. The organization of cholesteric spherulites. *Journal Physique*, 45:1899–1923, 1984.

[3] Emre Bukusoglu, Xiaoguang Wang, Jose A Martinez-Gonzalez, Juan J de Pablo, and Nicholas L Abbott. Stimuli-responsive cubosomes formed from blue phase liquid crystals. *Adv. Mater. (Weinheim, Ger.)*, 27(43):6892–6898, 2015.

[4] Emre Bukusoglu, Xiaoguang Wang, Ye Zhou, José A Martínez-González, Mohammad Rahimi, Qi Wang, Juan J de Pablo, and Nicholas L Abbott. Positioning colloids at the surfaces of cholesteric liquid crystal droplets. *Soft matter*, 12(42):8781–8789, 2016.

[5] S. Chandrasekhar. *Liquid Crystals*. Cambridge University Press, 2 edition, 1992.

[6] Simon Čopar, Tine Porenta, and Slobodan Žumer. Visualisation methods for complex nematic fields. *Liq. Cryst.*, 40(12):1759–1768, 2013.

[7] Simon Čopar, Uroš Tkalec, Igor Muševič, and Slobodan Žumer. Knot theory realizations in nematic colloids. *Proceedings of the National Academy of Sciences*, 112(6):1675–1680, 2015.

[8] Alexandre Darmon, Michael Benzaquen, David Seč, Simon Čopar, Olivier Dauchot, and Teresa Lopez-Leon. Waltzing route toward double-helix formation in cholesteric shells. *Proceedings of the National Academy of Sciences*, 113(34):9469–9474, 2016.

[9] Masao Doi. *Soft Matter Physics*. Oxford University Press, 2013.

[10] L Faget, S Lamarque-Forget, Ph Martinot-Lagarde, P Auroy, and I Dozov. Anticonical anchoring and surface transitions in a nematic liquid crystal. *Physical Review E*, 74(5):050701, 2006.

[11] Alberto Fernández-Nieves, Vincenzo Vitelli, Andrew S Utada, Darren R Link, Manuel Márquez, David R Nelson, and David A Weitz. Novel defect structures in nematic liquid crystal shells. *Physical review letters*, 99(15):157801, 2007.

[12] J-B Fournier and Paolo Galatola. Modeling planar degenerate wetting and anchoring in nematic liquid crystals. *EPL (Europhysics Letters)*, 72(3):403, 2005.

[13] Jun-ichi Fukuda and Slobodan Žumer. Quasi-two-dimensional skyrmion lattices in a chiral nematic liquid crystal. *Nat. Commun.*, 2:246, 2011.

[14] Mohamed Amine Gharbi, David Seč, Teresa Lopez-Leon, Maurizio Nobili, Miha Ravnik, Slobodan Žumer, and Christophe Blanc. Microparticles confined to a nematic liquid crystal shell. *Soft Matter*, 9(29):6911–6920, 2013.

[15] Yuedong Gu and Nicholas L Abbott. Observation of saturn-ring defects around solid microspheres in nematic liquid crystals. *Physical Review Letters*, 85(22):4719, 2000.

[16] Jugal K Gupta, Sri Sivakumar, Frank Caruso, and Nicholas L Abbott. Size-dependent ordering of liquid crystals observed in polymeric capsules with micrometer and smaller diameters. *Angew. Chem., Int. Ed.*, 48(9):1652–1655, 2009.

[17] SI Hernández, JA Moreno-Razo, A Ramírez-Hernández, E Díaz-Herrera, JP Hernández-Ortiz, and JJ de Pablo. Liquid crystal nanodroplets, and the balance between bulk and interfacial interactions. *Soft Matter*, 8(5):1443–1450, 2012.

[18] M Humar and I Muševič. 3d microlasers from self-assembled cholesteric liquid-crystal microdroplets. *Optics Express*, 18(26):26995–27003, 2010.

[19] Emine Kemiklioglu and Liang-Chy Chien. Polymer-encapsulated blue phase liquid crystal droplets. *Appl. Phys. Express*, 7(9):091701, 2014.

[20] Heinz Kitzerow and Christian Bahr. *Chirality in Liquid Crystals*. Springer Science & Business Media, 2001.

[21] M Kléman and C Williams. Anchoring energies and the nucleation of surface disclination lines in nematics. *Philos. Mag.*, 28(3):725–732, 1973.

[22] Vinzenz Koning, Teresa Lopez-Leon, Alexandre Darmon, Alberto Fernandez-Nieves, and Vincenzo Vitelli. Spherical nematic shells with a threefold valence. *Physical Review E*, 94(1):012703, 2016.

[23] MV Kurik and OD Lavrentovich. Negative-positive monopole transitions in cholesteric liquid crystals. *Journal of Experimental and Theoretical Physics Letters*, 35(9):444–447, 1982.

[24] Clayton P Lapointe, Thomas G Mason, and Ivan I Smalyukh. Shape-controlled colloidal interactions in nematic liquid crystals. *Science*, 326(5956):1083–1086, 2009.

[25] I-Hsin Lin, Daniel S Miller, Paul J Bertics, Christopher J Murphy, Juan J de Pablo, and Nicholas L Abbott. Endotoxin-induced structural transformations in liquid crystalline droplets. *Science*, 332(6035):1297–1300, 2011.

[26] T Lopez-Leon and A Fernandez-Nieves. Topological transformations in bipolar shells of nematic liquid crystals. *Physical Review E*, 79(2):021707, 2009.

[27] Teresa Lopez-Leon, Martin A Bates, and Alberto Fernandez-Nieves. Defect coalescence in spherical nematic shells. *Physical Review E*, 86(3):030702, 2012.

[28] Teresa Lopez-Leon and Alberto Fernandez-Nieves. Drops and shells of liquid crystal. *Colloid and Polym. Sci.*, 289(4):345–359, 2011.

[29] Teresa Lopez-Leon, V Koning, KBS Devaiah, Vincenzo Vitelli, and A Fernandez-Nieves. Frustrated nematic order in spherical geometries. *Nature Physics*, 7(5):391–394, 2011.

[30] JC Loudet and P Poulin. Application of an electric field to colloidal particles suspended in a liquid-crystal solvent. *Physical Review Letters*, 87(16):165503, 2001.

[31] Jean-Christophe Loudet, Philippe Barois, and Philippe Poulin. Colloidal ordering from phase separation in a liquid-crystalline continuous phase. *Nature*, 407(6804):611–613, 2000.

[32] TC Lubensky, David Pettey, Nathan Currier, and Holger Stark. Topological defects and interactions in nematic emulsions. *Physical Review E*, 57(1):610, 1998.

[33] TC Lubensky and Jacques Prost. Orientational order and vesicle shape. *Journal de Physique II*, 2(3):371–382, 1992.

[34] José A Martínez-González, Ye Zhou, Mohammad Rahimi, Emre Bukusoglu, Nicholas L Abbott, and Juan J de Pablo. Blue-phase liquid crystal droplets. *Proc. Natl. Acad. Sci. U. S. A.*, page 201514251, 2015.

[35] Daniel S Miller, Xiaoguang Wang, and Nicholas L Abbott. Design of functional materials based on liquid crystalline droplets. *Chem. Mater.*, 26(1):496–506, 2013.

[36] JA Moreno-Razo, EJ Sambriski, NL Abbott, JP Hernández-Ortiz, and JJ De Pablo. Liquid-crystal-mediated self-assembly at nanodroplet interfaces. *Nature*, 485(7396):86–89, 2012.

[37] Mohammad Reza Mozaffari, Mehrtash Babadi, Jun-ichi Fukuda, and Mohammad Reza Ejtehadi. Interaction of spherical colloidal particles in nematic media with degenerate planar anchoring. *Soft Matter*, 7(3):1107–1113, 2011.

[38] Harids Mundoor, Bohdan Senyuk, and Ivan I Smalyukh. Triclinic nematic colloidal crystals from competing elastic and electrostatic interactions. *Science*, 352(6281):69–73, 2016.

[39] Igor Muševič. Optical manipulation and self-assembly of nematic colloids: colloidal crystals and superstructures. *Liquid Crystals Today*, 19(1):2–12, 2010.

[40] Igor Muševič. Integrated and topological liquid crystal photonics. *Liq. Cryst.*, 41(3):418–429, 2014.

[41] Igor Muševič, Miha Škarabot, Uroš Tkalec, Miha Ravnik, and Slobodan Žumer. Two-dimensional nematic colloidal crystals self-assembled by topological defects. *Science*, 313(5789):954–958, 2006.

[42] Igor Muševič and Slobodan Žumer. Liquid crystals: maximizing memory. *Nature materials*, 10(4):266–268, 2011.

[43] VG Nazarenko, AB Nych, and BI Lev. Crystal structure in nematic emulsion. *Phys. Rev. Lett.*, 87(7):075504, 2001.

[44] David R Nelson. Toward a tetravalent chemistry of colloids. *Nano Letters*, 2(10):1125–1129, 2002.

[45] M Nobili and G Durand. Disorientation-induced disordering at a nematic-liquid-crystal–solid interface. *Physical Review A*, 46(10):R6174, 1992.

[46] Andriy Nych, Ulyana Ognysta, Miha Škarabot, Miha Ravnik, Slobodan Žumer, and Igor Muševič. Assembly and control of 3d nematic dipolar colloidal crystals. *Nature Communications*, 4:1489, 2013.

[47] Renate Ondris-Crawford, Evan P Boyko, Brian G Wagner, John H Erdmann, Slobodan Žumer, and J William Doane. Microscope textures of nematic droplets in polymer dispersed liquid crystals. *Journal of applied physics*, 69(9):6380–6386, 1991.

[48] Tetiana Orlova, Sarah Jane Aßhoff, Tadatsugu Yamaguchi, Nathalie Katsonis, and Etienne Brasselet. Creation and manipulation of topological states in chiral nematic microspheres. *Nat. Commun.*, 6:1–9, 2015.

[49] J. Prost P. G. de Gernnes. *The physics of liquid crystals*. Oxford university press, 1995.

[50] David Pires, Jean-Baptiste Fleury, and Yves Galerne. Colloid particles in the interaction field of a disclination line in a nematic phase. *Phys. Rev. Lett.*, 98(24):247801, 2007.

[51] H Poincaré. Reprinted in oeuvres de henri poincaré, i. *J. de Math. Pures Appl.*, 1:167, 1885.

[52] Philippe Poulin, Holger Stark, TC Lubensky, and DA Weitz. Novel colloidal interactions in anisotropic fluids. *Science*, 275(5307):1770–1773, 1997.

[53] Mohammad Rahimi, Tyler F Roberts, Julio C Armas-Pérez, Xiaoguang Wang, Emre Bukusoglu, Nicholas L Abbott, and Juan J de Pablo. Nanoparticle self-assembly at the interface of liquid crystal droplets. *Proc. Natl. Acad. Sci. U. S. A.*, 112(17):5297–5302, 2015.

[54] Sriram Ramaswamy, Rajaram Nityananda, VA Raghunathan, and Jacques Prost. Power-law forces between particles in a nematic. *Molecular Crystals and Liquid Crystals*, 288(1):175–180, 1996.

[55] O Ou Ramdane, Ph Auroy, S Forget, E Raspaud, Ph Martinot-Lagarde, and I Dozov. Memory-free conic anchoring of liquid crystals on a solid substrate. *Physical Review Letters*, 84(17):3871, 2000.

[56] Miha Ravnik and Slobodan Žumer. Landau–de gennes modelling of nematic liquid crystal colloids. *Liquid Crystals*, 36(10-11):1201–1214, 2009.

[57] RW Ruhwandl and EM Terentjev. Long-range forces and aggregation of colloid particles in a nematic liquid crystal. *Physical Review E*, 55(3):2958, 1997.

[58] E. G. Virga S. Kralj, R. Rosso. Curvature control of valence on nematic shells. *Soft matter*, 2011.

[59] David Seč, Teresa Lopez-Leon, Maurizio Nobili, Christophe Blanc, Alberto Fernandez-Nieves, Miha Ravnik, and Slobodan Žumer. Defect trajectories in nematic shells: Role of elastic anisotropy and thickness heterogeneity. *Physical Review E*, 86(2):020705, 2012.

[60] David Seč, Tine Porenta, Miha Ravnik, and Slobodan Žumer. Geometrical frustration of chiral ordering in cholesteric droplets. *Soft Matter*, 8(48):11982–11988, 2012.

[61] Bohdan Senyuk, Qingkun Liu, Sailing He, Randall D Kamien, Robert B Kusner, Tom C Lubensky, and Ivan I Smalyukh. Topological colloids. *Nature*, 493(7431):200, 2013.

[62] Bohdan Senyuk, Owen Puls, M Tovkach, Stanislav B Chernyshuk, and Ivan I Smalyukh. Hexadecapolar colloids. *Nature communications*, 7, 2016.

[63] V Sergan and G Durand. Anchoring anisotropy of a nematic liquid crystal on a bistable sio evaporated surface. *Liquid Crystals*, 18(1):171–174, 1995.

[64] Seyed Reza Seyednejad, Mohammad Reza Mozaffari, and Mohammad Reza Ejtehadi. Confined nematic liquid crystal between two spherical boundaries with planar anchoring. *Physical Review E*, 88(1):012508, 2013.

[65] Homin Shin, Mark J Bowick, and Xiangjun Xing. Topological defects in spherical nematics. *Physical review letters*, 101(3):037802, 2008.

[66] Gregor Skačej and Claudio Zannoni. Controlling surface defect valence in colloids. *Physical review letters*, 100(19):197802, 2008.

[67] Miha Škarabot, Miha Ravnik, Slobodan Žumer, Uroš Tkalec, Igor Poberaj, Dušan Babič, and Igor Muševič. Hierarchical self-assembly of nematic colloidal superstructures. *Phys. Rev. E*, 77(6):061706, 2008.

[68] Piotr Sleczkowski, Ye Zhou, Supitchaya Iamsaard, Juan J de Pablo, Nathalie Katsonis, and Emmanuelle Lacaze. Light-activated helical inversion in cholesteric liquid crystal microdroplets. *Proceedings of the National Academy of Sciences*, page 201720742, 2018.

[69] Ivan I Smalyukh, S Chernyshuk, BI Lev, AB Nych, U Ognysta, VG Nazarenko, and OD Lavrentovich. Ordered droplet structures at the liquid crystal surface and elastic-capillary colloidal interactions. *Phys. Rev. Lett.*, 93(11):117801, 2004.

[70] Ivan I Smalyukh, O D Lavrentovich, A N Kuzmin, A V Kachynski, and P N Prasad. Elasticity-mediated self-organization and colloidal interactions of solid spheres with tangential anchoring in a nematic liquid crystal. *Physical Review Letters*, 95(15):157801, 2005.

[71] Holger Stark. Physics of colloidal dispersions in nematic liquid crystals. *Physics Reports*, 351(6):387–474, 2001.

[72] Holger Stark. Saturn-ring defects around microspheres suspended in nematic liquid crystals: an analogy between confined geometries and magnetic fields. *Physical Review E*, 66(3):032701, 2002.

[73] Iain W Stewart. *The static and dynamic continuum theory of liquid crystals*, volume 17. Taylor and Francis, London, 2004.

[74] RP Trivedi, D Engström, and I I Smalyukh. Optical manipulation of colloids and defect structures in anisotropic liquid crystal fluids. *Journal of Optics*, 13(4):044001, 2011.

[75] AS Utada, El Lorenceau, DR Link, PD Kaplan, HA Stone, and DA Weitz. Monodisperse double emulsions generated from a microcapillary device. *Science*, 308(5721):537–541, 2005.

[76] Vincenzo Vitelli and David R Nelson. Nematic textures in spherical shells. *Physical Review E*, 74(2):021711, 2006.

[77] Charlie R Wand and Martin A Bates. Monte carlo simulations of nematic and chiral nematic shells. *Physical Review E*, 91(1):012502, 2015.

[78] Xiaoguang Wang, Daniel S Miller, Juan J de Pablo, and Nicholas L Abbott. Reversible switching of liquid crystalline order permits synthesis of homogeneous populations of dipolar patchy microparticles. *Adv. Funct. Mater.*, 24(39):6219–6226, 2014.

[79] Jonathan K Whitmer, Xiaoguang Wang, Frederic Mondiot, Daniel S Miller, Nicholas L Abbott, and Juan J de Pablo. Nematic-field-driven positioning of particles in liquid crystal droplets. *Phys. Rev. Lett.*, 111(22):227801, 2013.

[80] F Xu and PP Crooker. Chiral nematic droplets with parallel surface anchoring. *Phys. Rev. E*, 56(6):6853, 1997.

[81] Makoto Yada, Jun Yamamoto, and Hiroshi Yokoyama. Direct observation of anisotropic interparticle forces in nematic colloids with optical tweezers. *Physical Review Letters*, 92(18):185501, 2004.

[82] Ye Zhou, Emre Bukusoglu, José A Martínez-González, Mohammad Rahimi, Tyler F Roberts, Rui Zhang, Xiaoguang Wang, Nicholas L Abbott, and Juan J de Pablo. Structural transitions in cholesteric liquid crystal droplets. *ACS nano*, 2016.

[83] Ye Zhou, Ashley Guo, Rui Zhang, Julio C Armas-Perez, José A Martínez-González, Mohammad Rahimi, Monirosadat Sadati, and Juan J de Pablo. Mesoscale structure of chiral nematic shells. *Soft matter*, 12(44):8983–8989, 2016.